Non-hydrostatic, non-linear processes in the surf zone

Kévin Martins, Philippe Bonneton, Arthur Mouragues, Bruno Castelle

Non-hydrostatic, non-linear processes in the surf zone

Kévin Martins[1], **Philippe Bonneton**[1], **Arthur Mouragues**[1], **Bruno Castelle**[1]

[1]UMR 5805 EPOC, CNRS - Université de Bordeaux, Allée Geoffroy Saint-Hilaire, F-33615 Pessac, France

Key Points:

- Sub-surface pressure and lidar data are used to study the non-linear and non-hydrostatic character of surf zone waves
- Non-hydrostatic effects are strong even in the inner surf zone, where broken waves are sharp-crested and have a steep front
- Oscillatory flow under broken waves is dominated by irrotational motions

Corresponding author: K. Martins, kevin.martins@u-bordeaux.fr

Abstract

In the surf zone, non-hydrostatic processes are either neglected or estimated using linear wave theory. The recent development of technologies capable of directly measuring the free surface elevation, such as 2D lidar scanners, allow for a thorough assessment of the validity of such hypotheses. In this study, we use sub-surface pressure and lidar data to study the non-linear and non-hydrostatic character of surf zone waves. Non-hydrostatic effects are found important everywhere in the surf zone (from the outer to the inner surf zones). Surface elevation variance, skewness and asymmetry estimated from the hydrostatic reconstruction are found to significantly underestimate the values obtained from the lidar data. At the wave-by-wave scale, this is explained by the underestimation of the wave crest maximal elevations, even in the inner surf zone, where the wave profile around the broken wave face is smoothed. The classic transfer function based on linear wave theory brings only marginal improvements in this regard, compared to the hydrostatic reconstruction. A recently developed non-linear weakly dispersive reconstruction is found to consistently outperform the hydrostatic or classic transfer function reconstructions over the entire surf zone, with relative errors on the surface elevation variance and skewness around 5% on average. In both the outer and inner surf zones, this method correctly reproduces the steep front of breaking and broken waves, and their individual wave height to within 10%. The performance of this irrotational method supports the hypothesis that the flow under broken waves is dominated by irrotational motions.

Plain Language Summary

In the surf zone, waves undergo rapid changes in shape, passing from steep and skewed waves right before breaking to sawtooth-shaped asymmetric bores. Capturing and understanding these changes is crucial for coastal researchers and engineers since the breaking wave-induced hydrodynamics shape beaches at various temporal and spatial scales. In this study, we use lidar scanners and pressure sensors to study the non-hydrostatic and non-linear character of surf zone waves. We show that non-hydrostatic effects remain strong over the entire surf zone, i.e. fluid accelerations are important and the hypothesis of a hydrostatic pressure field leads to large deviations of the real surface elevation. More specifically, wave crests elevation are underestimated, and the sharp-crested shape of broken waves is rounded-off. A recently developed non-linear weakly dispersive method to reconstruct the free surface from sub-surface pressure is found to consistently outperform the hydrostatic or classic transfer function reconstructions over the entire surf zone, with relative errors on the surface elevation variance (related to the wave energy) and skewness (related to wave shape) around 5% on average. The performance of this irrotational method supports the hypothesis that the flow under broken waves is dominated by irrotational motions.

1 Introduction

In the surf zone, waves undergo rapid changes in shape, passing from steep and skewed waves right before breaking to sawtooth-shaped asymmetric bores in what is referred to as the inner surf zone (e.g., Basco, 1985; Battjes, 1988). Most of the energy dissipated during breaking processes is transferred to the water column through mixing (Ting and Kirby, 1996; Drazen and Melville, 2009), induces a wave setup near the shoreline (e.g., Longuet-Higgins and Stewart, 1964; Stive and Wind, 1982; Apotsos et al., 2007; Guérin et al., 2018) and forces the circulation of the nearshore (e.g., see Svendsen, 1984; Deigaard et al., 1991; Peregrine and Bokhove, 1998; Feddersen et al., 1998; Bühler and Jacobson, 2001; Bonneton et al., 2010; Castelle et al., 2016). Wave-induced nearshore circulation shape beaches at various temporal and spatial scales (Wright and Short, 1984) and are also important for cross-shelf exchanges of sediment, pollutants and nutrients (e.g., Shanks et al., 2010). In addition, wave orbital velocity skewness and asymmetry, which result from wave shape changes in the nearshore, drive a net onshore sediment transport (Hoefel and Elgar, 2003) and are therefore key to pattern and rate of beach recovery after storms. Measuring accurately the complex changes that waves exhibit around and after the breaking point is thus critical to coastal engineers and researchers.

The problem of measuring waves can be simply viewed as our capacity to detect the air/water interface along with its spatial and temporal evolution. The surf zone is characterized by turbulent flows where breaking waves entrain large volumes of air in the water column, so that, at almost every stage of the wave propagation (under the wave front, crest and trough), air bubbles can be found at various concentrations near and under the free surface (Cox and Shin, 2003; Mori et al., 2007; Kimmoun and Branger, 2007). Directly measuring the free surface of breaking waves in the field is thus a challenging task, and seminal studies on surf zone wave kinematics mainly focused on the development of such measurement techniques (e.g., see Thornton et al., 1976). Although capacitance-type of wave gauges showed good skill in the field to measure the free surface, pressure sensors rapidly became the most commonly used approach for measuring waves in the surf zone, as they are robust and relatively cheap. However, retrieving the free surface from pressure measured at the bottom poses mathematical challenges, especially in the surf zone, where waves are highly non-linear.

The surf zone is generally divided into two regions: the outer surf zone, where waves break, and the inner surf zone, where most waves propagate as quasi-steady bores (Basco, 1985; Svendsen et al., 1978). Close to breaking, waves exhibit steep faces and, even after breaking, are characterized by strong vertical accelerations (e.g., see van Dorn, 1978; Elgar et al., 1988), which explains why non-hydrostatic effects are important in this region (see illustration in Figure 1a). In the inner surf zone, non-hydrostatic processes are generally assumed to be negligible (e.g., Raubenheimer et al., 1996; Sénéchal et al., 2001), due to the resemblance of broken waves with bores, under which the pressure field is very close to be hydrostatic (Madsen and Svendsen, 1983). Non-hydrostatic effects typically concentrate in the vicinity of the broken wave front (see illustration in Figure 1b), and have two main origins: 1) the vertical acceleration associated with the wave motion and 2) the roller structure where the flow is highly turbulent and strongly non-uniform in the vertical (e.g., see Govender et al., 2002). The numerical investigations of Lin and Liu (1998) for instance suggest that the assumption of a hydrostatic pressure field shows deviations of the free surface less than 10% under the crest of broken waves. Elsewhere (e.g. trough region), the fluid motions are near-horizontal and the hypothesis of a hydrostatic pressure field yields good estimates of the free surface elevation (Stive, 1980). Nonetheless, experimental data described in van Dorn (1978) show that 20-30% of error on the crest elevation can be expected in

the inner surf zone with the hydrostatic hypothesis, which is unacceptable for many coastal applications.

The supposedly negligible non-hydrostatic effects in the inner surf zone encouraged researchers to use the non-linear shallow water equations (NSWE) to simulate wave propagation in the inner surf zone (Kobayashi et al., 1989; Raubenheimer et al., 1996; Bonneton, 2007). This modelling approach, where the wave front is treated as a shock, reproduces quite well the non-linear distortion associated with saw-tooth waves in the surf zone, their celerity and the energy dissipation related to breaking processes (Bonneton, 2007). These encouraging results lead researchers to implement such hydrostatic shock-wave method in fully non-linear, non-hydrostatic models in order to deal with breaking and broken waves (e.g., Bonneton et al., 2011; Tissier et al., 2012; Shi et al., 2012; Smit et al., 2013). If these models provide a correct description of the global wave evolution, from the shoaling to the swash zone, their ability to properly reproduce non-hydrostatic wave processes in the entire surf zone remains questionable.

Early field studies also focused on the capacity of linear wave theory to correct for the depth-attenuation of the pressure signal and retrieve free surface and wave statistics elsewhere in the surf zone and in deeper water (e.g., Guza and Thornton, 1980; Thornton and Guza, 1983). Although wave-by-wave analyses were clearly not recommended (Bishop and Donelan, 1987), linear wave theory became the most common approach to reconstruct the free surface and retrieve wave characteristics from bottom-mounted pressure sensors (e.g., Sallenger Jr. and Holman, 1985; Elgar et al., 1997; Ruessink, 2010, and many others). Due to the need for cutoff frequencies, this approach does not allow spectral analyses to be performed at frequencies higher than approximately 3 to 4 times the peak frequency (typically $f < 0.3\,\mathrm{Hz}$), meaning that high harmonics, which reflect the degree of non-linearities, are not considered. The recent development of techniques capable of directly measuring the free surface based on acoustic (Bonneton et al., 2018; Mouragues et al., 2019) or lidar technology (Martins et al., 2017a) highlighted the limits of linear wave theory, which strongly underestimates the non-hydrostatic character of shoaling and breaking waves. This has implications in the estimates of surface elevation second (variance) and third-order (skewness and asymmetry) parameters as well as elevation extrema and distributions.

The present study has two main objectives: 1) Quantify the non-hydrostatic processes throughout the entire surf zone and 2) Apply the recently developed non-linear weakly dispersive reconstruction method of Bonneton et al. (2018) in the surf zone. We use sub-surface pressure data and direct measurements of the surface elevation obtained by lidar scanners previously collected in the field. The paper is organized as follows. In Section 2, we first briefly review the different field measuring techniques adapted to the surf zone. The three methods used in this paper to reconstruct the free surface from sub-surface pressure measurements (hydrostatic, linear and non-linear weakly dispersive) are also recalled. The different datasets collected at the macrotidal, dissipative site of Saltburn-by-the-Sea, UK, are presented in Section 3. In Section 4, we analyze the non-hydrostatic character of surf zone waves, in relation to their relative position in the surf zone (outer to inner surf zone). This is done by comparing surface elevation statistics (percentiles, second and third-order parameters) computed on the hydrostatic reconstruction with the direct measurements obtained from lidars. The three reconstruction methods considered here are then compared and their performances are analyzed in Section 5, in both the frequency and temporal domains. Finally, we summarize the different findings of this study in Section 6.

2 In situ methods for characterizing non-hydrostatic wave processes in the surf zone

2.1 Direct measurements of surf zone waves

Past field studies analyzed the cross-shore transformation of surf zone waves using visual estimates of the free surface obtained from a combination of video cameras and photopoles (Mizuguchi, 1982; Ebersole and Hughes, 1987). The presence of splashes around the poles (Ibaceta et al., 2018) and the errors associated with the pixel resolution limit the accuracy of the measurements to several centimeters in the surf zone. Although generally used in laboratory conditions (e.g., see Flick et al., 1981), capacitance and resistive types of wave gauges were used very early in the field to estimate surface elevation spectra in the shoaling region (Tucker and Charnock, 1954; Simpson, 1969; Flick et al., 1979) and in the surf zone (e.g., Thornton et al., 1976; Gonçalo, 1978; Thornton and Guza, 1983). More information on this type of gauges can be found in Flick et al. (1979), Shand et al. (2009) and the references therein. When calibrated, these gauges allow $O(\text{mm})$ accuracy in controlled environments, however, the presence of large pockets or fractions of air under breaking waves potentially leads to large errors in the estimation of the free surface, or at least its envelop. For instance, Kimmoun and Branger (2007) compared measurements from resistive gauges and PIV techniques, showing an underestimation of the surface elevation by the resistive gauges of up to 60% in the plunging and splash-up region, while the differences lied between 20 and 30% in the inner surf zone. This is explained by the working principle of resistive wave gauges whose response is proportional to the wire wet length. This cross-comparison between measuring techniques near the breaking point underlines the importance to consistently compare the same quantities, whether the comparisons are made between different measuring techniques or between numerical models and experimental data (e.g., see Lowe et al., 2019).

Acoustics sensors provide another method to detect the free surface, based on the time of flight technique. These can be deployed at the bottom of the water column (Pedersen et al., 2002; Birch et al., 2004; Mouragues et al., 2019) or above the surface (Turner et al., 2008), although the latter study focuses on the swash zone. When the air fraction along the water column is very small (i.e. no wave breaking), sub-surface acoustic sensors give very accurate estimates of the free surface elevation (e.g., see the comparisons with direct measurements from lidar scanners in Martins et al., 2017b). The presence of air bubbles associated with wave breaking processes prevents sound waves to reach the surface, hence making this method inappropriate for surf zone applications (Birch et al., 2004). In this case, bottom-mounted acoustic sensors would typically measure the lower bound of the surface roller structure (see illustration in Figure 1) or air pockets, which can be used in order to characterize breaking wave-induced air plumes in large scale experiments (Bryan et al., 2019).

As mentioned above, lidar scanners (mostly in the infrared spectrum) are capable of directly measuring the free surface, and are thus very powerful tools to study surf zone waves. The scanners can be stationed near the shoreline (Brodie et al., 2015; O'Dea et al., 2019) or mounted on structures such as temporary towers (Martins et al., 2016) or jetties (Martins et al., 2017c; Harry et al., 2018). 2D lidars provide highly-resolved, direct measurements of wave profiles which, as opposed to single-point sensors, allow the determination of geometric information about the wave shape, and its cross-shore evolution (e.g., on the roller angle and length, see Martins et al., 2018). Contrary to capacitance or resistive type of wave gauges, which can only underestimate the free surface elevation due to the presence of air fraction, lidar scanners provide the surface elevation envelope. Note that the application of lidars is not limited to the field since they can also be used during small (Blenkinsopp et al., 2012) and large scale (Vousdoukas et al., 2014; Martins et al., 2017a) laboratory experiments. Finally, few studies used photogrammetry techniques and data from colocated video cameras

to reconstruct the sea surface elevation and gain new insights into the directional properties of wave spectra in relatively deep water (Benetazzo, 2006; Peureux et al., 2018). Although these techniques show great promises, especially in terms of spatial resolution and coverage, its application to nearshore, breaking waves remains scarce (de Vries et al., 2011; Filipot et al., 2019), which is likely due to the experimental set-up and the data processing procedures that entail many technical complications (e.g. time synchronization).

2.2 Sub-surface pressure measurements of surf zone waves

Pressure sensors have always represented a cheap and robust solution to measure water waves in the nearshore, with studies dating back to the 40s (Folsom, 1947; Seiwell, 1947). However, as mentioned earlier, reconstructing the free surface from pressure measured is challenging, especially under strongly non-linear waves such as in the surf zone. The recent development of remote sensing methods capable of directly measuring surf zone waves is not only explained by technological advances, but is also motivated by the need to obtain reliable and accurate measurements where pressure sensors and the classic surface reconstruction methods fail. Mouragues et al. (2019) give a recent review on the different methods to reconstruct the free surface from sub-surface pressure measurements, with an application to shoaling waves. Below, we recall the three most commonly used methods for practical nearshore applications: the hydrostatic reconstruction ('hyd'), the classic transfer function method (based on linear wave theory, 'lin') and the non-linear weakly dispersive reconstruction method ('snl') recently derived in Bonneton et al. (2018).

The main hypothesis used to derive the linear and non-linear weakly dispersive formula is that the flow is irrotational. Here, it is important to note that these two methods correct the non-hydrostatic effects associated with the irrotational part of the wave flow. Hence, none of these methods are designed to estimate the non-hydrostatic effects related to the roller, which is the aerated and turbulent structure located at the broken wave face (Figure 1). For more information on their derivation, the reader is referred to Bonneton and Lannes (2017), Bonneton et al. (2018) and Mouragues et al. (2019).

Hydrostatic reconstruction.

Neglecting the vertical acceleration in the momentum equation yields the hydrostatic reconstruction of the free surface:

$$\zeta_{\mathrm{hyd}} = \frac{P_{\mathrm{m}} - P_{\mathrm{atm}}}{\rho g} + \delta_{\mathrm{m}} - h_0, \tag{1}$$

where P_{m} is the pressure measured at a distance δ_{m} from the bed, P_{atm} is the atmospheric pressure, ρ is the water density, g is the gravity constant and h_0 is the mean water depth. Note that the different variables used throughout the paper are listed in Table 1.

The hypothesis of a hydrostatic pressure field gives good estimate of the free surface elevation for very long waves such as tidal waves, which are characterized by a very small dispersion (or shallowness) parameter μ (with $\mu = kh_0$, where h_0 is the mean water depth and k is the wave number). Note that contrary to Bonneton and Lannes (2017), Bonneton et al. (2018) and Mouragues et al. (2019), we choose, for the sake of readability, to define μ without the power 2. In opposite to long waves, short waves propagating in the nearshore exhibit rather steep faces, characterized by strong fluid accelerations. Hence, large errors on the reconstructed surface are expected in the shoaling and surf zones, especially close to the breaking point (e.g., see van Dorn, 1978).

Classic transfer function method.

The classic transfer method uses linear wave theory to approximate the velocity potential time derivative (e.g., see Bishop and Donelan, 1987). This can be written:

$$\mathcal{F}\{\zeta_{\mathrm{lin}}\}(\omega) = K_{p,\mathrm{lin}}(\omega)\mathcal{F}\{\zeta_{\mathrm{hyd}}\}(\omega) \quad (2)$$

$$K_{p,\,\mathrm{lin}}(\omega) = \frac{\cosh(kh_0)}{\cosh(k\delta_m)} \quad (3)$$

$$\omega^2 = gk\tanh(kh_0), \quad (4)$$

where ω is the radial frequency and $\mathcal{F}\{\cdot\}$ is the Fourier transform. Eq. 4 corresponds to the dispersion relation given by linear wave theory, and is used in Eq. 3 to compute the correction factor applied to the hydrostatic reconstruction in Eq. 2 (in the frequency space). Reconstructing the surface elevation using the transfer function method given by linear wave theory (Eq. 2-4) yields good estimates of bulk parameters for linear waves (e.g., Hom-ma et al., 1966; Esteva and Harris, 1970; Grace, 1978; Cavaleri, 1980, and many others) as long as adequate deployment procedures and analyses techniques are used (Bishop and Donelan, 1987).

As wave non-linearities increase in shallow depths, the classic transfer function written in Eq. 2 needs a cutoff frequency in order to avoid the overestimation of the correction factor K_p at relatively high frequencies (e.g., $f > 0.4f_p$, with f_p the peak frequency), see for instance Gonçalo (1978) and Mouragues et al. (2019). This overestimation was generally attributed to the presence of noise in the pressure measurements (e.g., Guza and Thornton, 1980; Jones and Monismith, 2007, and many others). Bonneton and Lannes (2017) and Bonneton et al. (2018) show that the reason why the transfer function from linear wave theory blows up is in fact due to wave non-linearities and the presence of secondary harmonics. These harmonics are phase-locked (bound) to the primary wave and their wave number is thus largely overestimated when using the dispersion relation from linear wave theory given in Eq. 4 (see Bonneton and Lannes, 2017). This is supported by the analyses from Lee and Wang (1984) and the recent application of the non-linear weakly dispersive formula by Mouragues et al. (2019). The need for a cutoff frequency prevents the accurate description of high harmonics, meaning that sharp-crested waves cannot be accurately described and their wave height and skewness are generally largely underestimated (e.g., Martins et al., 2017a; Bonneton et al., 2018; Mouragues et al., 2019).

Non-linear weakly dispersive reconstruction.

Bonneton and Lannes (2017) presented a fully-dispersive non-linear reconstruction method that yields better description of second and third-order moments of fully-dispersive wave groups compared to linear wave theory or other non-linear reconstructions such as the heuristic method by Vasan and Oliveras (2017). Building on this work, Bonneton et al. (2018) derived a non-linear formula for weakly dispersive waves ($\mu^2 \lesssim 0.3$) which reads:

$$\zeta_{\mathrm{sl}} = \zeta_{\mathrm{hyd}} - \frac{h_0}{2g}(1-(\delta_m/h_0)^2)\frac{\partial^2\zeta_{\mathrm{hyd}}}{\partial t^2} \quad (5)$$

$$\zeta_{\mathrm{snl}} = \zeta_{\mathrm{sl}} - \frac{1}{g}\left(\frac{\partial}{\partial t}\left(\zeta_{\mathrm{sl}}\frac{\partial\zeta_{\mathrm{sl}}}{\partial t}\right) - (\delta_m/h_0)^2\left(\frac{\partial\zeta_{\mathrm{sl}}}{\partial t}\right)^2\right) \quad (6)$$

where ζ_{sl} is a linear shallow water reconstruction upon which the non-linear reconstruction ζ_{snl} is based. Unlike the transfer function method (Eq. 2), the non-linear formula of Eq. 6 does not use the dispersion relation, meaning that the cutoff frequency can be much higher (Bonneton et al., 2018; Mouragues et al., 2019). This implies that the shape of non-linear waves propagating in the shoaling region or near the breaking point can be better described. Similarly, free surface high-order moments are also more accurately estimated in these regions (Bonneton et al., 2018; Mouragues et al., 2019).

The fact that the non-linear formula (Eq. 6) uses and corrects a linear reconstruction (Eq. 5) explains why the non-linear reconstruction can still be sensitive to wave non-linearities and might require a cutoff frequency smaller than the frequency where noise dominates in the pressure data. This point is of relevance for coastal applications, and will be further discussed in Section 5 and in the Appendix for the present application in the surf zone. Finally, it is worth noting that the time-averaged surface elevation predicted by the non-linear reconstruction method is similar to that of the hydrostatic reconstruction, i.e. $\langle \zeta_{\mathrm{snl}} \rangle = \langle \zeta_{\mathrm{hyd}} \rangle$ (with $\langle \cdot \rangle$ the time-averaging operator).

3 Methods

3.1 Study site and field data

The present study uses lidar and pressure data collected during the field experiments performed at Saltburn-by-the-Sea, UK (Figure 2a) during April 2016 (Martins et al., 2017c, 2018). Similar to Martins et al. (2017c, 2018), we only use data from 9-10 April 2016, corresponding to a swell event characterized by a peak wave period $T_{\mathrm{p}} = 9 - 11\,\mathrm{s}$ and a significant wave height $H_{\mathrm{s}} = 1\,\mathrm{m}$. During these two days, a mean peak wave direction of 16.9° NE was measured at the nearshore buoy deployed in 17-m depth, with a directional spread of 15.3°. Since the coastline around the pier is oriented towards 18° NE, incident waves were essentially propagating shore normal and parallel to the pier. The Saltburn beach is dissipative ($\tan\beta \sim 1:65$) and presents a macrotidal regime, with a mean tidal range of 5.2 m measured at the Whitby tidal gauge during the period of interest, see Figure 2a for location.

During these experiments, three eye-safe 2-D lidar scanners (SICK LMS511, $\lambda = 904\,\mathrm{nm}$) were deployed along the pier to measure the time-varying free surface elevation of shoaling, breaking and broken waves at 25 Hz (Figures 2b and 2c). Three Nortek Acoustic Doppler Velocimeters (ADVs) were deployed at three distinct cross-shore locations (Figure 2c) to measure current velocities several centimeters ($\sim 10\,\mathrm{cm}$) above the seabed. Near-bed pressure was measured at these locations by three pressure transducers (PT) deployed vertically and synchronized with the ADVs. The most seaward and the middle PTs corresponded to external GE Druck PTX1830 sensors, while the most landward PT corresponded to the internal pressure sensor from the third ADV. Both pressure and current data were collected at 16 Hz. Although the beach experienced very little morphological change throughout the experiment, the distance between the pressure sensor and the bed level was measured at every low tide for surface reconstruction purposes. Similarly, the ADVs' head position were monitored, and if needed, were repositioned to maintain the $\sim$ 10-cm distance above the seabed. Finally, an additional pressure transducer was deployed at the seaward limit of the pier in order to measure local wave conditions outside the surf zone. The data from this PT was also used to estimate the peak period, later used to compute the local wave number k with the linear dispersion relation (Eq. 4).

3.2 Data processing

Time series of pressure and surface elevation directly measured by the lidar were organized in bursts of 512 s. The lidar data was first re-sampled at 16 Hz to match the pressure time frame. Each of the burst time series were linearly detrended to remove the tidal component. Note that this is the only signal processing that was applied to the time series as no low/high-pass filters were used.

As noted above, two of the pressure transducers were external sensors, designed to work in shallow environments (maximum depth of 10 m) while the internal pressure sensor from the most landward ADV was designed to work in deeper water (100-m depth). This is an important detail as much higher noise was present in the measure-

ments from the Nortek PT, which prevented the analysis of the pressure time series at high frequencies. Hence, the data from that particular PT was disregarded. Bursts where the lidar data had more than 10% non-return signal (before re-sampling) were also disregarded. This only concerned the data at the location of the middle ADV, since it was located between two scanners. In this region, the lidar scanners need the persistent presence of foam to return a continuous signal. On the contrary, a continuous return signal was obtained by the lidar at the most seaward PT, even in the absence of breaking events, as it is located closer to nadir.

As the burst data covered several hours of the tidal cycles, it is important for the present analysis to qualitatively know in which region of the surf zone waves were propagating. This was accomplished by visually estimating Q_b, the fraction of breaking and broken waves at the ADV location from the lidar data. Following Martins et al. (2017c), waves were considered breaking at the ADV location only when the first features associated with breaking processes (e.g. splashes, active wave face) could already be detected at that position. The results of this detection are presented in Figure 3, in which we can observe a linear trend between Q_b and $\langle\zeta^2\rangle$, the surface elevation variance measured by the lidar. As in the surf zone, the surface elevation variance is largely dictated by the water depth, Figure 3 also reveals the controlling effect of the water depth on Q_b. The data points are coloured by the relative water depth μ, which, as a dispersive parameter, characterizes the non-hydrostatic effect. The smallest μ values coincide with the lowest $\langle\zeta^2\rangle$ values and correspond to the boundary between the inner surf zone and the swash zone, which was dominated by infragravity waves. The presence of small waves carried by these low-frequency motions explain why the breaking fraction is not 1 for the lowest μ values. The largest μ values, which coincide with the highest $\langle\zeta^2\rangle$, correspond to the boundary between the outer surf zone and the shoaling region, where the largest waves first break. The scatter observed in Figure 3 can be explained by the slight inter-tidal variations in wave conditions observed during the two days considered here (Martins et al., 2017c) as well as by the natural variation of Q_b in natural surf zones (e.g., see the recent study of Stringari and Power, 2019).

In the remainder of the paper, we thus use the shallowness parameter μ as an indicator of the relative position in the surf zone. The non-hydrostatic and non-linear character of the surf zone waves monitored at Saltburn are studied using second (variance) and third-order surface elevation parameters (skewness and asymmetry). If $\zeta(t)$ denotes the free surface elevation at one spatial location, with t the time, these quantities can be defined as follows:

$$\begin{aligned} \text{Variance}: \quad & \langle(\zeta - \langle\zeta\rangle)^2\rangle \\ \text{Skewness}: \quad S_k = \quad & \frac{\langle(\zeta - \langle\zeta\rangle)^3\rangle}{\langle(\zeta - \langle\zeta\rangle)^2\rangle^{3/2}} \\ \text{Asymmetry}: \quad A_s = \quad & \frac{\langle(\mathcal{H}\left(\zeta - \langle\zeta\rangle\right))^3\rangle}{\langle(\zeta - \langle\zeta\rangle)^2\rangle^{3/2}} \end{aligned}$$

where $\mathcal{H}(\cdot)$ is the Hilbert transform. The variance of the surface elevation is associated to the wave energy, while its skewness and asymmetry characterize the vertical (peaked) and horizontal (pitched forward) asymmetry of the wave form respectively.

4 Non-hydrostatic wave processes in the surf zone

In this section, we quantify the non-hydrostatic character of surf zone waves by comparing statistics and bulk parameters computed on the hydrostatic reconstruction (ζ_{hyd}, Eq. 1) with the direct measure from the lidar scanners (ζ_{lidar}).

4.1 Bulk and high-order surface elevation parameters

We first compare the 5% and 95% percentiles $\zeta_{5\%}$ and $\zeta_{95\%}$ of the two surface elevation datasets. $\zeta_{5\%}$ represents the lower 5% of the surface elevation time series for each burst, hence corresponding to wave troughs while $\zeta_{95\%}$ represents the highest 5% of the surface elevation time series, hence corresponding to the highest wave crests of the burst. The fact that $\zeta_{\mathrm{lidar},5\%}$ and $\zeta_{\mathrm{hyd},5\%}$ follow the 1:1 line in the present dataset (Figure 4a) means that the pressure field is mostly hydrostatic around wave troughs in the entire surf zone, which is in agreement with past experimental and numerical studies (e.g., van Dorn, 1978; Stive, 1980; Lin and Liu, 1998). In contrast, $\zeta_{\mathrm{hyd},95\%}$ consistently underestimates $\zeta_{\mathrm{lidar},95\%}$ (Figure 4b): the relative differences, computed here as 100 x $|\zeta_{\mathrm{lidar},95\%} - \zeta_{\mathrm{hyd},95\%}|/\zeta_{\mathrm{lidar},95\%}$, decrease from 15-20% in the outer surf zone to approximately 5% in the inner surf zone. This suggests that the hydrostatic reconstruction underestimates the elevation of the highest wave crests, independently from the relative position in the surf zone.

Next, we present in Figure 5a the comparison of the variance of the two surface elevation datasets for the 52 bursts analyzed here. The hydrostatic reconstruction is found to consistently underestimate the free surface elevation variance, and hence the wave energy in the surf zone. In the outer surf zone ($\mu > 0.26$), the hydrostatic reconstruction underestimates the elevation variance by up to 30%; this is expected since breaking waves are characterized by rapid vertical acceleration under the crest (e.g., van Dorn, 1978; Hieu et al., 2004). For values down to $\mu \sim 0.20$, non-hydrostatic effects remain strong, as seen in the relatively constant underestimation of the surface elevation variance by the hydrostatic reconstruction (between 25-30%). Only in the inner surf zone, which corresponds to $\mu < 0.16$ in the present dataset, we observe differences of approximately 10% in the elevation variance and thus less non-hydrostatic effects. It can be noted that the variation of the relative error with the non-dimensioned water depth is in qualitative agreement with the experimental data from van Dorn (1978).

Third-order parameters of ζ_{hyd} also display large relative differences compared to the lidar data. The skewness $S_{k,\,\mathrm{hyd}}$ of the surface elevation reconstructed from the hydrostatic assumption underestimates the values obtained from the lidar data $S_{k,\,\mathrm{lidar}}$ by $\sim 40-50\%$, independently from the relative water depth (Figure 5b). This strong underestimation of the wave skewness is at least partly explained by the fact that wave crest elevations are consistently underestimated throughout the surf zone, even when most waves are broken (Figure 4b). Compared to $S_{k,\,\mathrm{hyd}}$, the asymmetry $A_{s,\,\mathrm{hyd}}$ presents a slightly different behavior. $A_{s,\,\mathrm{hyd}}$ exhibits large relative differences compared to the free surface elevation asymmetry $A_{k,\,\mathrm{lidar}}$, which decreases linearly with μ (Figure 5c). The relative differences are approximately 45% for $\mu > 0.26$ and decreases to approximately 25% in the inner surf zone, for $\mu < 0.16$. Overall, these large differences indicate that non-hydrostatic processes are important for the estimation of high-order surface elevation parameters. The large underestimation of the wave asymmetry in the inner surf zone is particularly surprising as one would expect the hydrostatic reconstruction to be more accurate in describing the sawtooth shape of long, broken waves, which are typical of inner surf zones. This point will be further analyzed in Section 5.

4.2 Spectral shape and influence of a cutoff frequency on bulk parameters

To better understand the errors made in the shallowest parts of the surf zone, below we isolate a burst corresponding to waves propagating in the inner surf zone ($\mu = 0.17$ and $> 90\%$ of waves are broken, i.e. $Q_b > 0.9$).

Figure 6 shows the energy density spectra S_ζ computed for both ζ_{hyd} and ζ_{lidar} over this particular burst. Two energy peaks can be observed from these spectra. A

first peak at $f = 0.02\,\mathrm{Hz}$ corresponds to the infragravity motions dominating the inner surf and swash zones during the experiments. The second peak, located at $f = 0.1\,\mathrm{Hz}$, corresponds to the peak frequency f_p of the incident short waves, which at this stage of their propagation in the surf zone suffered much dissipation. Up to $f \approx 0.3\,\mathrm{Hz}$, both spectra exhibit similar shapes and levels of energy (Figure 6). However, large differences on the spectra tails are observed for higher frequencies. The energy density spectrum evaluated from ζ_{lidar} displays a f^{-2} tail, characteristic of inner surf zone waves (Kaihatu et al., 2007), while that evaluated from ζ_{hyd} displays a $f^{-7/2}$ tail, which is, to the best of our knowledge, an undocumented behavior.

To analyze the effect of the differences in the tail shape and energy levels on surface elevation bulk parameters, we investigate the effect of a potential cutoff frequency f_c on the computation of these parameters. This was done by computing, for varying f_c, the bulk parameters on the surface elevation signals that were low-pass filtered at f_c with a Fourier-type filter. The results are shown in Figure 7. Up to $f \sim 0.2\,\mathrm{Hz}$ (twice the incident wave peak frequency), there are no differences between the parameters computed from ζ_{hyd} and ζ_{lidar}. All parameters computed on ζ_{hyd} reach relatively stable values at $f \sim 0.6\,\mathrm{Hz}$, with little variations when the cutoff is applied at higher frequencies. This is explained by the much lower energy levels contained at those frequencies in $S_{\zeta,\,\mathrm{hyd}}$ compared to $S_{\zeta,\,\mathrm{lidar}}$ (Figure 6). The divergence of the bulk parameters computed from ζ_{hyd} and ζ_{lidar} with varying f_c emerge from the differences in energy levels between 0.4 and 1 Hz, which is related to different surface elevation spectral tails. The final relative errors for this burst are 8%, 52% and 26% for the surface elevation variance (Figure 7a), skewness (Figure 7b) and asymmetry (Figure 7c) respectively. Overall, these results suggest that, in the inner surf zone at least, non-hydrostatic effects concentrate in the high frequency part of the elevation spectrum ($f > 2 - 3f_p$). These results also confirm the importance of incorporating spectral information at high-frequencies in order to accurately describe second and third-order surface elevation parameters, even in the inner surf zone. This is particularly true for the wave skewness, which is very sensitive to the choice of f_c. For instance, $f_c = 3f_p$ only leads to a value approximately half the real value.

5 Application of the reconstruction methods in the surf zone

The results from the previous section show that the spectral information at high frequencies ($f > 3f_p$) is needed in order to accurately estimate the surface elevation variance, skewness and asymmetry from sub-surface pressure measurements. In this section, we apply the different reconstruction methods introduced earlier, and in particular the non-linear weakly dispersive reconstruction method of Bonneton et al. (2018), to the surf zone data collected at Saltburn.

For the present analysis, we isolate a burst corresponding to waves propagating in the transitional region of the shoaling region and the outer surf zone, so that, with the inner surf zone burst of Section 4, they represent the two extremes of the present dataset. The outer surf zone burst is characterized by $h_0 = 2.15\,\mathrm{m}$, $\mu = 0.29$ and a fraction of broken and breaking waves estimated at 9% ($Q_b \sim 0.09$).

5.1 Spectral domain

Figures 8a and 8b show the energy density spectra S_ζ of the different reconstructed surface elevation signals for the outer and inner surf zone cases respectively. In this Figure, we also show the equivalent transfer functions K_p for each of the reconstruction (Figures 8c and 8d); these were computed as $K_{p,\,\mathrm{lin}} = S_{\zeta,\,\mathrm{lin}}/S_{\zeta,\,\mathrm{hyd}}$ and $K_{p,\,\mathrm{snl}} = S_{\zeta,\,\mathrm{snl}}/S_{\zeta,\,\mathrm{hyd}}$ for the linear and non-linear reconstruction respectively. These equivalent transfer functions are compared against the ground truth ratio $S_{\zeta,\,\mathrm{lidar}}/S_{\zeta,\,\mathrm{hyd}}$,

which effectively represents the transfer function required to pass from the hydrostatic reconstruction to the lidar data. In practice, this is the target transfer function.

Compared to the inner surf zone case, the energy density spectra from the outer surf zone burst displays quite different behaviours. In the outer surf zone, the energy peak corresponds to the incident short wave peak frequency $f_p = 0.1\,\mathrm{Hz}$ (Figure 8a). $S_{\zeta,\,\mathrm{hyd}}$ is shown to underestimate the energy levels starting from the second harmonic only ($f = 0.2\,\mathrm{Hz}$), while in the inner surf zone, the differences between $S_{\zeta,\,\mathrm{hyd}}$ and $S_{\zeta,\,\mathrm{lidar}}$ remain small up to the fourth harmonic (Figure 8b). The latter point can also be observed in the good match between second and third-order parameters computed on the hydrostatic and lidar signals for $f_c < 0.4\,\mathrm{Hz}$ (Figure 7). In the spectrum tail, the difference between $S_{\zeta,\,\mathrm{hyd}}$ and $S_{\zeta,\,\mathrm{lidar}}$ is even larger for the outer surf zone case and reaches two orders of magnitude for $f > 0.6\,\mathrm{Hz}$.

In Figures 8a and 8b, two signals reconstructed with the transfer function from linear theory (Eq. 3) are shown: a signal without cutoff frequency ζ_{lin}, and $\zeta_{\mathrm{lin,\,f_c}}$, a signal to which a cutoff $f_{c,\,\mathrm{lin}}$ was applied at frequencies where the transfer function starts to blow up. Without cutoff frequency, $S_{\zeta,\,\mathrm{lin}}$ deviates quite rapidly from $S_{\zeta,\,\mathrm{lidar}}$ in both the outer (Figure 8a) and inner surf zone cases (Figure 8b). The levels of energy corrected with linear wave theory are almost one order of magnitude too high around $f = 0.6\,\mathrm{Hz}$ in the outer surf zone ($K_{p,\,\mathrm{lin}} \sim 100$, Figure 8c), while this range of error is only reached at $f = 1\,\mathrm{Hz}$ in the inner surf zone (Figure 8d). As these frequencies are much lower than the frequency where noise in the measurements is dominant ($f \sim 1.2\,\mathrm{Hz}$, see Appendix), we here provide more evidence that a cutoff frequency is needed with linear wave theory because of wave non-linearity and not only because of the presence of noise in the measurements. By analyzing the ratio $S_{\zeta,\,\mathrm{lidar}}/S_{\zeta,\,\mathrm{hyd}}$ in Figure 8c and 8d, $K_{p,\,\mathrm{lin}}$ can be considered inappropriate starting from $f \sim 0.4\,\mathrm{Hz}$ in the outer surf zone while this occurs around $f \sim 0.5\,\mathrm{Hz}$ in the inner surf zone. These frequencies were thus chosen as cutoff frequency $f_{c,\,\mathrm{lin}}$ to compute $\zeta_{\mathrm{lin,\,f_c}}$.

The use of a cutoff frequency in the linear reconstruction has slightly different consequences depending on the relative position in the surf zone. In the outer surf zone, the large differences in energy levels between $S_{\zeta,\mathrm{hyd}}$ and $S_{\zeta,\mathrm{lidar}}$ at frequencies between 0.2 and 0.4 Hz (Figure 8a) lead to considerable improvements of the estimates of wave parameters when using the linear reconstruction compared to the hydrostatic reconstruction (see Table 2). The error on the variance is reduced from 25.5% to 5.8% in the outer surf zone, compared to an improvement of only 6% in the inner surf zone (although, the error made with the hydrostatic reconstruction is already low, see Table 3). As already seen in Figure 7, the need for a cutoff frequency limits the accuracy in the computation of third-order moments. Here, the relative errors on third-order moments for $\zeta_{\mathrm{lin,\,f_c}}$ remain above 30% in the outer surf zone and above 17% in the inner surf zone. In the inner surf zone, the difference in energy levels between $S_{\zeta,\,\mathrm{lidar}}$ and $S_{\zeta,\,\mathrm{hyd}}$ are much smaller, which explains why the transfer function from linear wave theory only brings marginal improvement compared to the hydrostatic reconstruction due to the cutoff frequency (Table 3). This also explains why the hypothesis of a hydrostatic pressure field was sometimes made in the inner surf zone (Sénéchal et al., 2001).

For the two particular cases analyzed here, the non-linear weakly dispersive method of Bonneton et al. (2018) uses cutoff frequencies at least twice that used by the transfer function from linear wave theory. For the outer surf zone burst, $f_{\mathrm{c,\,snl}} = 0.9\,\mathrm{Hz}$ (Figure 8a) while we use $f_{\mathrm{c,\,snl}} = 1.1\,\mathrm{Hz}$ in the inner surf zone (Figure 8b). As explained in the Appendix, imposing $f_{\mathrm{c,\,snl}} = 1.1\,\mathrm{Hz}$ is close to be the upper limit for any burst from the present dataset, as noise in the pressure measurements becomes dominant at higher frequencies. The lower cutoff frequency used in the outer surf zone case is required due to important wave non-linearities. This is explained by the fact

that the non-linear method introduced by Bonneton et al. (2018) corrects the signal reconstructed using linear wave theory (cf. Eq. 5 and 6), which is sensitive to the choice of $f_{c,\,\mathrm{snl}}$. This point is further discussed in the Appendix, especially from a practical point of view. The fact that cutoff frequencies can be taken almost up to where the noise in the measurements is strong allows the non-linear reconstruction method to reach equivalent transfer function corrections of $O(10^2)$ in the outer surf zone (see around $f = 1\,\mathrm{Hz}$ in Figure 8c) and $O(10)$ in the inner surf zone (for $f > 1\,\mathrm{Hz}$, see Figure 8d). For both cases, the correction coefficients match those corresponding to the ratio $S_{\zeta,\,\mathrm{lidar}}/S_{\zeta,\,\mathrm{hyd}}$, meaning that the non-linear reconstruction correctly reproduces the energy levels up to $f = 1.2\,\mathrm{Hz}$ (Figure 8). In the outer surf zone, the corresponding relative error on the variance is close to 0%, while the error on the wave skewness and asymmetry is as low as 5.7% and 14.9% respectively (Table 2). In the inner surf zone (Figure 8b), the surface spectrum tail is well captured by the non-linear reconstruction, and leads to similar performances for bulk parameters estimates (relative errors $< 6\%$ for all parameters, see Table 3). These can even be improved by imposing a lower cutoff frequency (around 1 Hz), but the spectra tails do not match anymore.

5.2 Temporal domain

Figure 9 shows the propagation of a wave group extracted from the outer surf zone case. The capacity of the non-linear reconstruction to correctly represent the energy density spectrum tail reflects from the good representation of the wave crest elevations. This is not the case with the linear reconstruction, which consistently underestimates the maximum elevations, especially for the steepest waves. This is well illustrated with the fifth wave of the group, which is just about to break and can be considered as an extreme wave since $\zeta_c/H_s = 1.85$, where ζ_c is the crest elevation (e.g., see Dysthe et al., 2008). For this particular wave, the error on the crest elevation is approximately 35% with the linear reconstruction (Figure 9), a number which is consistent with Martins et al. (2017a) and Mouragues et al. (2019). As mentioned in the previous section, the cutoff frequencies for this example are $f_{c,\,\mathrm{lin}} = 0.4\,\mathrm{Hz}$ and $f_{c,\,\mathrm{snl}} = 0.9\,\mathrm{Hz}$.

A closer look at the extreme wave in the group is given in Figure 10. As observed in Figures 9 and 10b, the pressure field is mostly hydrostatic at the trough level; this is in agreement with the observations from Section 4. The neglect (hydrostatic reconstruction) or underestimation (linear reconstruction) of the fluid acceleration leads to an overestimation of the surface elevation ζ_{hyd} and $\zeta_{\mathrm{lin},\,\mathrm{f_c}}$ as the wave face approaches (Figure 10c). Under the crest, only the non-linear reconstruction can well approximate the sharp crested shape of the wave, while the linear reconstruction brings only little improvement compared to the hydrostatic reconstruction for such an extreme wave (Figures 10d and 10e). At the back of the wave, ζ_{hyd} and $\zeta_{\mathrm{lin},\,\mathrm{f_c}}$ tend to be overestimated, before matching well again the direct measurements at the following trough. In agreement with recent studies (e.g., see Bonneton et al., 2018), we find relative errors of 26.7% and 28.7% for the variance and skewness respectively, when computed on the surface elevation reconstructed with linear wave theory $\zeta_{\mathrm{lin},\,\mathrm{f_c}}$. These errors decrease to 7.6% and 6.0% respectively with the non-linear weakly dispersive method. Overall, these errors are well illustrated with the spatial transformation of the breaking wave shown by the lidar data, which highlights the volume of water missed near the crest with the hydrostatic and linear reconstructions (Figures 10b-g).

Comparisons of reconstructed surface elevation time series are also performed for the inner surf zone burst and are shown in Figure 11. In this region of the surf zone, the hydrodynamics is dominated by long, sawtooth-shaped, broken waves. Although most waves display an overall sawtooth shape, they also exhibit a sharp, small crest at the wave front (see for instance Figure 11b). These sharp crests are systematically missed

by the linear and hydrostatic reconstructions (Figure 11a). Furthermore, the zoom in Figure 11b demonstrates the very little differences between the two reconstructions, which is consistent with earlier observations and Table 3. Not only the crests are missed, but the front wave slope is smoothed, and explains why third-order moments are strongly underestimated with the hydrostatic and linear reconstruction methods, even in the inner surf zone. In contrast, the non-linear weakly dispersive reconstruction method shows great skill in describing the shapes of individual inner surf zone waves. Wave crests elevations are much better described compared to ζ_{hyd} and $\zeta_{\mathrm{lin},\,\mathrm{f_c}}$, and only the largest wave shows some underestimation of the real elevation (Figure 11b). Typical errors on individual wave heights over this burst decrease from approximately 20% with linear wave theory to around 10% for the largest waves. Further, the wave face slope is also much better described by the non-linear reconstruction, which is consistent with the match between $S_{\zeta,\,\mathrm{snl}}$ and $S_{\zeta,\,\mathrm{lidar}}$ at high frequencies. More importantly, this suggests that the hypothesis upon which the non-linear weakly dispersive formula is built, i.e. that the flow is irrotational, is applicable under broken waves.

5.3 Performances of the reconstruction methods

Figure 12 summarizes, for the present dataset, the performances of the different reconstruction methods to describe second (variance) and third-order (S_k and A_s) surface elevation bulk parameters. It is worth noting that in this Section, the cutoff frequencies $f_{\mathrm{c},\,\mathrm{lin}}$ and $f_{\mathrm{c},\,\mathrm{snl}}$ vary for each burst and were optimized by visually checking S_ζ.

Following the observations from Section 4, the relative difference on the surface elevation variance made with the hydrostatic reconstruction remains relatively constant (between 25 and 30%) for $\mu > 0.20$ (Figure 12a). It is only for $\mu < 0.20$, which corresponds to $Q_b > 0.7-0.8$, that the relative differences decrease. This suggests that non-hydrostatic effects are strong everywhere in the surf zone and weaken only when most waves are broken. Inappropriate definitions of the inner surf zone in regards to breaker indexes (e.g. when the occurrence of wave breaking is still important) or other wave parameters might hence lead to large errors on wave parameters estimates if the hydrostatic reconstruction is preferred over those regions (e.g., Sénéchal et al., 2001). Although it suffers from the need of a cutoff frequency, the transfer function based on linear wave theory systematically improves the estimates of the surface elevation variance to within 10% on average. It is worth noting that the wave energy in the inner surf zone is hence better described with linear wave theory than with the hydrostatic reconstruction, as long as the cutoff frequency is correctly chosen. Ultimately, using the non-linear weakly dispersive reconstruction method of Bonneton et al. (2018) leads to errors on the variance inferior to 5% on average, independently from the local water depth.

As opposed to the surface variance, third-order parameters (Figures 12b and 12c) are not much better predicted with linear wave theory. Compared to the hydrostatic reconstruction, the relative error on A_s is roughly halved (Figure 12c), while that on S_k is reduced by approximately 10% on average but remains high ($> 30\%$ on average) anywhere in the surf zone (Figure 12b). Except for $\mu \sim 0.24$, where the average error on A_s is approximately 15%, the non-linear weakly dispersive reconstruction leads to errors inferior to 5% on average for both parameters.

6 Conclusions

We use sub-surface pressure and surface elevation lidar data collected at the macrotidal, dissipative site of Saltburn-by-the-Sea, UK, to study the non-hydrostatic and non-linear character of surf zone waves. The results presented in Section 4 inform

us that non-hydrostatic effects remain important in the entire surf zone. In the inner surf zone, where the pressure field is generally assumed hydrostatic, the variance of the surface elevation computed on the hydrostatic reconstruction is underestimated by 10% on average (Figure 12a). Consistent with earlier observations, non-hydrostatic effects concentrate in a relatively small region around the wave face (see illustration in Figure 1) and have two consequences on the reconstructed wave profile: wave crests elevation are underestimated and the elevation profile near the broken wave front is smoothed. As a consequence, surface elevation skewness and asymmetry estimate on ζ_{hyd} show underestimations larger than 40% and 20% respectively in this region of the surf zone (Figures 12b and 12c), despite the fact that broken waves exhibit an overall sawtooth shape (e.g., see Figure 11).

As long as the cutoff frequency $f_{c,\,\mathrm{lin}}$ is carefully chosen, the transfer function based on linear wave theory improves the estimation of surface elevation bulk parameters over the entire surf zone (Figure 12). For instance, the variance of the surface elevation (and hence the energy) is correct within 10% on average, for optimised $f_{c,\,\mathrm{lin}}$. However, the cutoff frequency, needed to prevent the overestimation of the transfer function, is a severe constraint in the accurate representation of energy levels at frequencies higher than $f = 3 - 6f_p$ (Figures 7a and 7b). This results in an large underestimation of the wave crest elevation and third-order parameters, even in the inner surf zone, where we show that $\zeta_{\mathrm{lin,\,f_c}}$ also smooths the steep broken wave face profile (Figures 10a and 10b).

For optimised cutoff frequencies, the non-linear weakly dispersive formula from Bonneton et al. (2018) leads to relative errors of 5% on average for all parameters analyzed here (Figure 12), except for large μ where larger errors are obtained for the wave asymmetry. Note that in this region of the surf zone, the wave asymmetry is relatively small. The performances of this formula in the inner surf zone (Figure 11) demonstrate that the hypothesis of the flow being irrotational under broken waves is appropriate, which was not expected. These results also indirectly support the approach made by Lucarelli et al. (2018) that the bottom layer under spilling breakers is characterized by an irrotational flow. None of the reconstruction methods presented here account for the rotational and turbulent part of the flow, which concentrates around the active part of the breaker (surface roller, Figure 1). However, the performances of the non-linear formula demonstrate that these effects should have little impact on the dominant flow associated with the wave propagation. Similarly, the presence of large fractions of air near the broken wave face might only be perceived by the lidar, which could explain the slight underestimation of crest elevations in the reconstructed signals. Elsewhere in the surf zone, splashes generated by breaking were not found to have any effect on quantities derived from the lidar dataset, which is explained by the large variability in the breaking point location. Along with the use of the cutoff frequency $f_{c,\,\mathrm{snl}}$, non-hydrostatic effects from the roller and fundamental differences in the measuring techniques (around breaking and due to entrained air) might explain the differences obtained with the non-linear reconstruction method.

These findings open up several research perspectives for surf zone hydrodynamics, some of which are discussed here. The first point regards surf zone wave statistics obtained in the field with pressure sensors and linear wave theory, and possibly in some laboratory studies that employed resistive type of wave gauges (Section 2.1). Unlike the classic transfer function, the non-linear weakly dispersive formula is clearly adapted to wave-by-wave analyses and will allow the derivation of more accurate wave statistics in the field (e.g. wave height distribution and extrema). In particular, wave height distributions are used in most nearshore circulation models and are thus of paramount importance. The second point developed here regards the approach used to deal with wave breaking processes in fully non-linear, non-hydrostatic models. We have shown that intense non-hydrostatic wave effects are localized very closed to the turbulent wave

front (see Figure 1). This leads to great difficulties in modelling the localized energy dissipation without affecting the non-hydrostatic quasi-potential wave field. Hence, classical breaking parametrizations in fully non-linear non-hydrostatic models, either based turbulent viscosity or shock-wave approaches, tend to round-off the highest wave crests. For these reasons, it is crucial to improve breaking parametrizations in phase-resolving models.

Appendix A On the choice of the cutoff frequency f_c

To reconstruct the free surface elevation, both the classic transfer function method (Eq. 2) and the non-linear weakly dispersive reconstruction method (Eq. 6) need cut-off frequencies. In Section 5, the performances of these two reconstruction methods were assessed with optimized cutoff frequencies, meaning that the relative errors provided in this study are very close to the minimum errors that can be reached with the present dataset. In practice, the energy density of the free surface elevation is not known, and robust criterion are desirable for the pressure correction.

As described earlier in the manuscript, $f_{c,\,\mathrm{snl}}$ varied considerably in the surf zone, as a function of wave non-linearities. This is explained by the fact that the non-linear formula uses and corrects a linear, shallow water reconstruction that is still sensitive to wave non-linearities. For large μ in the present dataset, values down to 0.6-0.65 Hz were taken for $f_{c,\,\mathrm{snl}}$. These values correspond to bursts for which $f_{c,\,\mathrm{lin}}$ were the smallest (i.e. 0.35-0.40 Hz). It is worth noting that $f_{c,\,\mathrm{snl}}$ is systematically greater than $f_{c,\,\mathrm{lin}}$ by a factor between 1.5 and 2 in the present dataset. In other cases, noise in the pressure measurements is the most limiting factor. This noise, which can be identified where the elevation spectrum tail flattens (e.g., Smith, 2002), can have several origins: the power system, the pressure transducer or the flow disturbance (Cavaleri, 1980; Bishop and Donelan, 1987; Smith, 2002). Here, the noise level is easily identified in $S_{\zeta,\,\mathrm{hyd}}$ over the entire surf zone (see Figure A1, for the outer and inner surf zone bursts): the noise dominates at frequencies higher than approximately 1.2 Hz, which will be referred to as $f_{c,\,\mathrm{noise}}$ in the following. Similar to the data collected in the shoaling region by Bonneton et al. (2018) and Mouragues et al. (2019), noise in the pressure data is thus the limiting factor for some of the bursts, which are characterized by relatively low μ values, and for which $f_{c,\,\mathrm{snl}}$ was taken up to 1.2 Hz. $f_{c,\,\mathrm{noise}}$ defines the upper bound for $f_{c,\,\mathrm{snl}}$, however, it will differ with the type of pressure sensor used and will vary with the deployment procedures, the hydrodynamic conditions etc. Displaying surface elevation spectra as in Figure A1 can help defining an upper bound for the cutoff frequency.

For the linear transfer function (Eq. 3), Smith (2002) suggest that $f_{c,\,\mathrm{lin}}$ should be chosen so that $|K_{p,\,\mathrm{lin}}|^2 < 100 - 1000$. In Section 5, we show that $|K_{p,\,\mathrm{lin}}|^2 < 25 - 100$ and $|K_{p,\,\mathrm{lin}}|^2 < 4 - 10$ are the maximum range before the transfer function is overestimated for the outer and surf zone cases respectively (Figures 8c and 8d). This suggests that the validity range for $K_{p,\,\mathrm{lin}}$ varies with the relative water depth. Figure A2 shows the ratio $K_{p,\,\mathrm{lidar}} = S_{\zeta,\,\mathrm{lidar}}/S_{\zeta,\,\mathrm{hyd}}$ for every burst, which effectively represents the observed transfer function. The abrupt change of slope around $f = 1.2$ Hz confirms that above this frequency, the noise dominates the spectrum, since the correction should increase with f. Below this pivot frequency, $K_{p,\,\mathrm{lidar}}$ increases with μ, confirming the point made above. This also highlights the difficulty to define both $f_{c,\,\mathrm{lin}}$ and $f_{c,\,\mathrm{snl}}$ based on a threshold value in the corresponding transfer function.

For now, both $f_{c,\,\mathrm{lin}}$ and $f_{c,\,\mathrm{snl}}$ are best chosen by carefully looking at elevation spectral tails: when the chosen value is too high, slope changes in $S_{\zeta,\,\mathrm{lin}}$ and $S_{\zeta,\,\mathrm{snl}}$ tails can be witnessed. As seen in Figure 8, $f_{c,\,\mathrm{lin}}$ is easily chosen, since the change in the spectrum tail is very abrupt. The situation with the non-linear weakly dispersive reconstruction method is somewhat different, as quadratic interactions among

the fundamental modes fill the elevation spectrum beyond the cutoff frequency (Bonneton and Lannes, 2017). Hence, the slope change is much milder in the non-linear reconstruction compared to what is found for the linear reconstruction.

Acknowledgments

K. Martins greatly acknowledges the financial support from the University of Bordeaux, through an International Postdoctoral Grant (Idex, nb. 1024R-5030). The Ph.D. thesis work of A. Mouragues is cofunded by a DGA-Région Nouvelle-Aquitaine scholarship. The collection of the field data was possible only thanks to the financial support from the Engineering and Physical Sciences Research Council through the grant EP/N019237/1 "Waves in Shallow Water", awarded to Chris Blenkinsopp. Gerd Masselink, his team and the University of Plymouth, UK, are warmly thanked for letting us use two ADVs and external pressure sensors. The data used in this research can be accessed on Zenodo at http://doi.org/10.5281/zenodo.3351952 or from the corresponding author, and used under Creative Commons Attribution 4.0 International licence. The authors thank Ryan Lowe and one anonymous reviewer for their helpful comments and suggestions.

References

Apotsos, A., B. Raubenheimer, S. Elgar, R. T. Guza, and J. A. Smith (2007), Effects of wave rollers and bottom stress on wave setup, *Journal of Geophysical Research: Oceans*, *112*(C2), doi:10.1029/2006JC003549.

Basco, D. R. (1985), A qualitative description of wave breaking, *Journal of Waterway, Port, Coastal, and Ocean Engineering*, *111*(2), 171 – 188, doi:10.1061/(ASCE)0733-950X(1985)111:2(171).

Battjes, J. A. (1988), Surf-zone dynamics, *Annual Review of Fluid Mechanics*, *20*(1), 257 – 291, doi:10.1146/annurev.fl.20.010188.001353.

Benetazzo, A. (2006), Measurements of short water waves using stereo matched image sequences, *Coastal Engineering*, *53*(12), 1013 – 1032, doi:10.1016/j.coastaleng.2006.06.012.

Birch, R., D. B. Fissel, K. Borg, V. Lee, and D. English (2004), The capabilities of doppler current profilers for directional wave measurements in coastal and nearshore waters, in *Oceans '04 MTS/IEEE Techno-Ocean '04 (IEEE Cat. No.04CH37600)*, vol. 3, pp. 1418 – 1427, doi:10.1109/OCEANS.2004.1406330.

Bishop, C. T., and M. A. Donelan (1987), Measuring waves with pressure transducers, *Coastal Engineering*, *11*(4), 309 – 328, doi:10.1016/0378-3839(87)90031-7.

Blenkinsopp, C. E., I. L. Turner, M. J. Allis, W. L. Peirson, and L. E. Garden (2012), Application of lidar technology for measurement of time-varying free-surface profiles in a laboratory wave flume, *Coastal Engineering*, *68*, 1 – 5, doi:10.1016/j.coastaleng.2012.04.006.

Bonneton, P. (2007), Modelling of periodic wave transformation in the inner surf zone, *Ocean Engineering*, *34*(10), 1459 – 1471, doi:10.1016/j.oceaneng.2006.09.002.

Bonneton, P., and D. Lannes (2017), Recovering water wave elevation from pressure measurements, *Journal of Fluid Mechanics*, *833*, 399 – 429, doi:10.1017/jfm.2017.666.

Bonneton, P., N. Bruneau, B. Castelle, and F. Marche (2010), Large-scale vorticity generation due to dissipating waves in the surf zone, *Discrete & Continuous Dynamical Systems - B*, *13*(4), 729 – 738, doi:10.3934/dcdsb.2010.13.729.

Bonneton, P., E. Barthelemy, F. Chazel, R. Cienfuegos, D. Lannes, F. Marche, and M. Tissier (2011), Recent advances in Serre-Green Naghdi modelling for wave transformation, breaking and runup processes, *European Journal of Mechanics - B/Fluids*, *30*(6), 589 – 597, doi:10.1016/j.euromechflu.2011.02.005.

Bonneton, P., D. Lannes, K. Martins, and H. Michallet (2018), A nonlinear weakly dispersive method for recovering the elevation of irrotational surface waves from pressure measurements, *Coastal Engineering*, *138*, 1 – 8, doi:10.1016/j.coastaleng.2018.04.005.

Brodie, K. L., B. Raubenheimer, S. Elgar, R. K. Slocum, and J. E. McNinch (2015), Lidar and pressure measurements of inner-surfzone waves and setup, *Journal of Atmospheric and Oceanic Technology*, *32*(10), 1945 – 1959, doi:10.1175/JTECH-D-14-00222.1.

Bryan, O., P. M. Bayle, C. E. Blenkinsopp, and A. J. Hunter (2019), Breaking wave imaging using lidar and sonar, *IEEE Journal of Oceanic Engineering*, pp. 1 – 11, doi:10.1109/JOE.2019.2900967.

Bühler, O., and T. E. Jacobson (2001), Wave-driven currents and vortex dynamics on barred beaches, *Journal of Fluid Mechanics*, *449*, 313 – 339, doi:10.1017/S0022112001006322.

Castelle, B., T. Scott, R. W. Brander, and R. J. McCarroll (2016), Rip current types, circulation and hazard, *Earth-Science Reviews*, *163*, 1 – 21, doi:10.1016/j.earscirev.2016.09.008.

Cavaleri, L. (1980), Wave measurement using pressure transducer, *Oceanologica Acta*, *3*(3), 339 – 346.

Cox, D. T., and S. Shin (2003), Laboratory measurements of void fraction and turbulence in the bore region of surf zone waves, *J. Eng. Mech.*, *129*(10), 1197 – 1205, doi:10.1061/(ASCE)0733-9399(2003)129:10(1197).

de Vries, S., D. F. Hill, M. A. de Schipper, and M. J. F. Stive (2011), Remote sensing of surf zone waves using stereo imaging, *Coastal Engineering*, *58*(3), 239 – 250, doi:10.1016/j.coastaleng.2010.10.004.

Deigaard, R., P. Justesen, and J. Fredsøe (1991), Modelling of undertow by a one-equation turbulence model, *Coastal Engineering*, *15*(5), 431 – 458, doi:10.1016/0378-3839(91)90022-9.

Drazen, D. A., and W. K. Melville (2009), Turbulence and mixing in unsteady breaking surface waves, *Journal of Fluid Mechanics*, *628*, 85 – 119, doi:10.1017/S0022112009006120.

Dysthe, K., H. E. Krogstad, and P. Mller (2008), Oceanic rogue waves, *Annual Review of Fluid Mechanics*, *40*(1), 287 – 310, doi:10.1146/annurev.fluid.40.111406.102203.

Ebersole, B. A., and S. A. Hughes (1987), DUCK85 photopole field experiment, *Tech. rep.*, ADA188477, DTIC Document.

Elgar, S., R. T. Guza, and M. H. Freilich (1988), Eulerian measurements of horizontal accelerations in shoaling gravity waves, *Journal of Geophysical Research: Oceans*, *93*(C8), 9261 – 9269, doi:10.1029/JC093iC08p09261.

Elgar, S., R. T. Guza, B. Raubenheimer, T. H. C. Herbers, and E. L. Gallagher (1997), Spectral evolution of shoaling and breaking waves on a barred beach, *Journal of Geophysical Research: Oceans*, *102*(C7), 15,797 – 15,805, doi:10.1029/97JC01010.

Esteva, D., and D. Harris (1970), Comparison of pressure and staff wave gage records, in *Proceedings of the 12th Conference on Coastal Engineering, Washington, D.C.*, pp. 101 – 116.

Feddersen, F., R. T. Guza, S. Elgar, and T. H. C. Herbers (1998), Alongshore momentum balances in the nearshore, *Journal of Geophysical Research: Oceans*, *103*(C8), 15,667 – 15,676, doi:10.1029/98JC01270.

Filipot, J.-F., P. Guimaraes, F. Leckler, J. Hortsmann, R. Carrasco, E. Leroy, N. Fady, M. Accensi, M. Prevosto, R. Duarte, V. Roeber, A. Benetazzo, C. Raoult, M. Franzetti, A. Varing, and N. Le Dantec (2019), La jument lighthouse: a real-scale laboratory for the study of giant waves and their loading on marine structures, *Philosophical Transactions of the Royal Society A: Mathematical, Physical and Engineering Sciences*, *377*(2155), 20190,008, doi:10.1098/rsta.2019.0008.

Flick, R., R. Lowe, M. Freilich, and J. Boylls (1979), Coastal and laboratory wavestaff system, in *OCEANS '79*, pp. 623 – 625, doi:10.1109/OCEANS.1979.1151229.

Flick, R. E., R. T. Guza, and D. L. Inman (1981), Elevation and velocity measurements of laboratory shoaling waves, *Journal of Geophysical Research: Oceans*, *86*(C5), 4149–4160, doi:10.1029/JC086iC05p04149.

Folsom, R. G. (1947), Sub-surface pressures due to oscillatory waves, *Eos, Transactions American Geophysical Union*, *28*(6), 875 – 881, doi:10.1029/TR028i006p00875.

Gonçalo, V. M. H. (1978), Measuring shallow water waves with pressure sensors, Master's thesis, Naval Postgraduate School, Monterey, California.

Govender, K., G. P. Mocke, and M. J. Alport (2002), Video-imaged surf zone wave and roller structures and flow fields, *Journal of Geophysical Research: Oceans*, *107*(C7), 9–1 – 9–21, doi:10.1029/2000JC000755.

Grace, R. A. (1978), Surface wave heights from pressure records, *Coastal Engineering*, *2*, 55 – 67, doi:10.1016/0378-3839(78)90005-4.

Guérin, T., X. Bertin, T. Coulombier, and A. de Bakker (2018), Impacts of wave-induced circulation in the surf zone on wave setup, *Ocean Modelling*, *123*, 86 – 97, doi:10.1016/j.ocemod.2018.01.006.

Guza, R. T., and E. B. Thornton (1980), Local and shoaled comparisons of sea surface elevations, pressures, and velocities, *Journal of Geophysical Research: Oceans*, *85*(C3), 1524 – 1530, doi:10.1029/JC085iC03p01524.

Harry, M., H. Zhang, C. Lemckert, G. Colleter, and C. E. Blenkinsopp (2018), Observation of surf zone wave transformation using lidar, *Applied Ocean Research*, *78*, 88 – 98, doi:10.1016/j.apor.2018.05.015.

Hieu, P. D., T. Katsutoshi, and V. T. Ca (2004), Numerical simulation of breaking waves using a two-phase flow model, *Applied Mathematical Modelling*, *28*(11), 983 – 1005, doi:10.1016/j.apm.2004.03.003.

Hoefel, F., and S. Elgar (2003), Wave-induced sediment transport and sandbar migration, *Science*, *299*(5614), 1885 – 1887, doi:10.1126/science.1081448.

Hom-ma, M., K. Horikawa, and S. Komori (1966), Response characteristics of underwater wave gauge, in *Proceedings of 10th Conference on Coastal Engineering, Tokyo, Japan*, pp. 99 – 114.

Ibaceta, R., R. Almar, P. A. Catalán, C. E. Blenkinsopp, L. P. Almeida, and R. Cienfuegos (2018), Assessing the performance of a low-cost method for video-monitoring the water surface and bed level in the swash zone of natural beaches, *Remote Sensing*, *10*(1), doi:10.3390/rs10010049.

Jones, N. L., and S. G. Monismith (2007), Measuring short-period wind waves in a tidally forced environment with a subsurface pressure gauge, *Limnology and Oceanography: Methods*, *5*(10), 317–327, doi:10.4319/lom.2007.5.317.

Kaihatu, J. M., J. Veeramony, K. L. Edwards, and J. T. Kirby (2007), Asymptotic behavior of frequency and wave number spectra of nearshore shoaling and breaking waves, *Journal of Geophysical Research: Oceans*, *112*(C6), doi:10.1029/2006JC003817.

Kimmoun, O., and H. Branger (2007), A particle image velocimetry investigation on laboratory surf-zone breaking waves over a sloping beach, *Journal of Fluid Mechanics*, *588*, 353 – 397, doi:10.1017/S0022112007007641.

Kobayashi, N., G. S. DeSilva, and K. D. Watson (1989), Wave transformation and swash oscillation on gentle and steep slopes, *Journal of Geophysical Research: Oceans*, *94*(C1), 951 – 966, doi:10.1029/JC094iC01p00951.

Lee, D., and H. Wang (1984), Measurement of surface waves from subsurface gage, in *Proceedings of the 19th Conference on Coastal Engineering, Houston, Texas*, pp. 271 – 286.

Lin, P., and P. L. Liu (1998), A numerical study of breaking waves in the surf zone, *Journal of Fluid Mechanics*, *359*, 239 – 264, doi:10.1017/S002211209700846X.

Longuet-Higgins, M. S., and R. W. Stewart (1964), Radiation stresses in water waves; a physical discussion, with applications, *Deep Sea Research and Oceanographic Abstracts*, *11*(4), 529 – 562, doi:10.1016/0011-7471(64)90001-4.

Lowe, R. J., M. L. Buckley, C. Altomare, D. P. Rijnsdorp, Y. Yao, T. Suzuki, and J. D. Bricker (2019), Numerical simulations of surf zone wave dynamics using smoothed particle hydrodynamics, *Ocean Modelling*, *144*, 101,481, doi:10.1016/j.ocemod.2019.101481.

Lucarelli, A., C. Lugni, M. Falchi, M. Felli, and M. Brocchini (2018), Extra strain rates in an unsteady spilling breaking wave, *Scientific Reports*, *8*(13926), doi:10.1038/s41598-018-32307-3.

Madsen, P. A., and I. A. Svendsen (1983), Turbulent bores and hydraulic jumps, *Journal of Fluid Mechanics*, *129*, 1 – 25, doi:10.1017/S0022112083000622.

Martins, K., C. E. Blenkinsopp, and J. Zang (2016), Monitoring individual wave characteristics in the inner surf with a 2-dimensional laser scanner (LiDAR), *Journal of Sensors, 2016*, pp. 1 – 11, doi:10.1155/2016/7965431.

Martins, K., C. E. Blenkinsopp, R. Almar, and J. Zang (2017a), The influence of swash-based reflection on surf zone hydrodynamics: a wave-by-wave approach, *Coastal Engineering*, *122*, 27 – 43, doi:10.1016/j.coastaleng.2017.01.006.

Martins, K., P. Bonneton, F. Frappart, G. Detandt, N. Bonneton, and C. E. Blenkinsopp (2017b), High frequency field measurements of an undular bore using a 2D LiDAR scanner, *Remote Sensing*, *9*(5), doi:10.3390/rs9050462.

Martins, K., C. E. Blenkinsopp, H. E. Power, B. Bruder, J. A. Puleo, and E. W. J. Bergsma (2017c), High-resolution monitoring of wave transformation in the surf zone using a LiDAR scanner array, *Coastal Engineering*, *128*, 37 – 43, doi:10.1016/j.coastaleng.2017.07.007.

Martins, K., C. E. Blenkinsopp, R. Deigaard, and H. E. Power (2018), Energy dissipation in the inner surf zone: New insights from lidar-based roller geometry measurements, *Journal of Geophysical Research: Oceans*, *123*(5), 3386 – 3407, doi:10.1029/2017JC013369.

Mizuguchi, M. (1982), Individual wave analysis of irregular wave deformation in the nearshore zone, in *Proceedings of the 18th Conference on Coastal Engineering, Cape Town, South Africa*, pp. 485 – 504.

Mori, N., T. Suzuki, and S. Kakuno (2007), Experimental study of air bubbles and turbulence characteristics in the surf zone, *Journal of Geophysical Research: Oceans*, *112*(C5), doi:10.1029/2006JC003647.

Mouragues, A., P. Bonneton, D. Lannes, B. Castelle, and V. Marieu (2019), Field data-based evaluation of methods for recovering surface wave elevation from pressure measurements, *Coastal Engineering*, *150*, 147 – 159, doi:10.1016/j.coastaleng.2019.04.006.

O'Dea, A., K. L. Brodie, and P. Hartzell (2019), Continuous coastal monitoring with an automated terrestrial lidar scanner, *Journal of Marine Science and Engineering*, *7*(2), doi:10.3390/jmse7020037.

Pedersen, T., S. Nylund, and A. Dolle (2002), Wave height measurements using acoustic surface tracking, in *OCEANS '02 MTS/IEEE, Biloxi, MI, USA*, vol. 3, pp. 1747 – 1754, doi:10.1109/OCEANS.2002.1191898.

Peregrine, D. H., and O. Bokhove (1998), Vorticity and surf zone currents, in *Proceedings of the 26th Conference on Coastal Engineering, Copenhagen, Denmark*, pp. 745 – 748.

Peureux, C., A. Benetazzo, and F. Ardhuin (2018), Note on the directional properties of meter-scale gravity waves, *Ocean Science*, *14*(1), 41 – 52, doi:10.5194/os-14-41-2018.

Raubenheimer, B., R. T. Guza, and S. Elgar (1996), Wave transformation across the inner surf zone, *Journal of Geophysical Research: Oceans*, *101*(C11), 25,589 – 25,597.

Ruessink, B. G. (2010), Observations of turbulence within a natural surf zone, *Journal of Physical Oceanography*, *40*(12), 2696 – 2712, doi:10.1175/2010JPO4466.1.

Sallenger Jr., A. H., and R. A. Holman (1985), Wave energy saturation on a natural beach of variable slope, *Journal of Geophysical Research: Oceans*, *90*(C6), 11,939 – 11,944, doi:10.1029/JC090iC06p11939.

Seiwell, H. R. (1947), Investigation of underwater pressure records and simultaneous sea surface patterns, *Eos, Transactions American Geophysical Union*, *28*(5), 722 – 724, doi:10.1029/TR028i005p00722.

Sénéchal, N., H. Dupuis, P. Bonneton, H. Howa, and R. Pedreros (2001), Observation of irregular wave transformation in the surf zone over a gently sloping sandy beach on the french atlantic coastline, *Oceanologica Acta*, *24*(6), 545 – 556, doi:10.1016/S0399-1784(01)01171-9.

Shand, T. D., W. L. Peirson, D. G. Bailey, and R. J. Cox (2009), Optical measurements of breaking wave water profiles, *Tech. rep.*, University of New South Wales, Water Research Laboratory: Research Report 236.

Shanks, A. L., S. G. Morgan, J. MacMahan, and A. J. H. M. Reniers (2010), Surf zone physical and morphological regime as determinants of temporal and spatial variation in larval recruitment, *Journal of Experimental Marine Biology and Ecology*, *392*(1), 140 – 150, doi:10.1016/j.jembe.2010.04.018, the Biology of Barnacles' in honour of Margaret Barnes.

Shi, F., J. T. Kirby, J. C. Harris, J. D. Geiman, and S. T. Grilli (2012), A high-order adaptive time-stepping TVD solver for Boussinesq modeling of breaking waves and coastal inundation, *Ocean Modelling*, *43 – 44*, 36 – 51, doi:10.1016/j.ocemod.2011.12.004.

Simpson, J. H. (1969), Observations of the Directional Characteristics of Sea Waves, *Geophysical Journal International*, *17*(1), 93 – 120, doi:10.1111/j.1365-246X.1969.tb06380.x.

Smit, P., M. Zijlema, and G. Stelling (2013), Depth-induced wave breaking in a non-hydrostatic, near-shore wave model, *Coastal Engineering*, *76*, 1 – 16, doi:10.1016/j.coastaleng.2013.01.008.

Smith, J. M. (2002), Wave pressure gauge analysis with current, *Journal of Waterway, Port, Coastal, and Ocean Engineering*, *128*(6), 271 – 275, doi:10.1061/(ASCE)0733-950X(2002)128:6(271).

Stive, M. J. F. (1980), Velocity and pressure field of spilling breakers, in *Proceedings of the 17th Conference on Coastal Engineering, Sydney, Australia*, pp. 547 – 566.

Stive, M. J. F., and H. G. Wind (1982), A study of radiation stress and set-up in the nearshore region, *Coastal Engineering*, *6*(1), 1 – 25, doi:10.1016/0378-3839(82)90012-6.

Stringari, C. E., and H. E. Power (2019), The fraction of broken waves in natural surf zones, *Journal of Geophysical Research: Oceans*, *n/a*(n/a), doi:10.1029/2019JC015213.

Svendsen, I. A. (1984), Mass flux and undertow in a surf zone, *Coastal Engineering*, *8*(4), 347 – 365, doi:10.1016/0378-3839(84)90030-9.

Svendsen, I. A., P. A. Madsen, and J. Buhr Hansen (1978), Wave characteristics in the surf zone, in *Proceedings of the 16th Conference on Coastal Engineering, Hamburg, Germany*, pp. 520 – 539.

Thornton, E. B., and R. T. Guza (1983), Transformation of wave height distribution, *Journal of Geophysical Research: Oceans*, *88*(C10), 5925 – 5938, doi:10.1029/JC088iC10p05925.

Thornton, E. B., J. J. Galvin, F. L. Bub, and D. P. Richardson (1976), Kinematics of breaking waves, in *Proceedings of the 15th Conference on Coastal Engineering, Honolulu, Hawaii*, pp. 461 – 476.

Ting, F. C., and J. T. Kirby (1996), Dynamics of surf-zone turbulence in a spilling breaker, *Coastal Engineering*, *27*(3), 131 – 160, doi:10.1016/0378-3839(95)00037-2.

998 Tissier, M., P. Bonneton, F. Marche, F. Chazel, and D. Lannes (2012), A new approach
999 to handle wave breaking in fully non-linear Boussinesq models, *Coastal Engineering*,
1000 *67*, 54 – 66, doi:10.1016/j.coastaleng.2012.04.004.
1001 Tucker, M. J., and H. Charnock (1954), A capacitance-wire recorder for small waves, in
1002 *Proceedings of the 5th Conference on Coastal Engineering, Grenoble, France*, p. 14.
1003 Turner, I. L., P. E. Russell, and T. Butt (2008), Measurement of wave-by-wave bed-
1004 levels in the swash zone, *Coastal Engineering*, *55*(12), 1237 – 1242, doi:10.1016/j.
1005 coastaleng.2008.09.009.
1006 van Dorn, W. G. (1978), Breaking invariants in shoaling waves, *Journal of Geophysical*
1007 *Research: Oceans*, *83*(C6), 2981 – 2988, doi:10.1029/JC083iC06p02981.
1008 Vasan, V., and K. L. Oliveras (2017), Water-wave profiles from pressure measurements:
1009 Extensions, *Applied Mathematics Letters*, *68*, 175 – 180, doi:10.1016/j.aml.2017.01.
1010 017.
1011 Vousdoukas, M. I., T. Kirupakaramoorthy, H. Oumeraci, M. de la Torre, F. Wübbold,
1012 B. Wagner, and S. Schimmels (2014), The role of combined laser scanning and video
1013 techniques in monitoring wave-by-wave swash zone processes, *Coastal Engineering*,
1014 *83*, 150 – 165, doi:10.1016/j.coastaleng.2013.10.013.
1015 Wright, L. D., and A. D. Short (1984), Morphodynamic variability of surf zones and
1016 beaches: A synthesis, *Marine Geology*, *56*(1), 93 – 118, doi:10.1016/0025-3227(84)
1017 90008-2.

Tables

Table 1. List of symbols. For the variables associated with the different reconstruction methods (ζ, K_p and f_c), we use the subscript 'hyd', 'lin' and 'snl' to refer to the hydrostatic (Eq. 1), linear (Eq. 2) and non-linear (Eq. 6) reconstruction methods respectively. The subscript 'lidar' refers to the direct lidar measurements.

Symbol	Description	Unit
$\tan\beta$	beach slope	-
δ_m	height of the pressure sensor above the bed	m
ζ	free surface elevation	m
ζ_c	wave crest elevation	m
μ	dispersion (shallowness) parameter ($\mu = kh_0$)	-
ω	radial frequency	rad.s^{-1}
f	frequency	s^{-1}
f_c	cutoff frequency	s^{-1}
f_p	peak wave frequency	s^{-1}
g	acceleration of gravity	m.s^{-2}
h_0	mean water depth	m
H	wave height	m
H_s	significant wave height	m
k	wave number	rad.m^{-1}
K_p	Transfer function	-
t	time	s
T	wave period	s
T_p	peak wave period	s
x	horizontal coordinate	m
z	vertical coordinate	m

Table 2. Relative errors made by the different reconstruction methods for the outer surf zone burst (Figure 8a, $h_0 = 2.15\,\mathrm{m}$, $\mu = 0.29$ and $H_s = 1.10\,\mathrm{m}$). For this burst, the cutoff frequencies used are $f_{\mathrm{c,\,lin}} = 0.4\,\mathrm{Hz}$ for the linear reconstruction and $f_{\mathrm{c,\,snl}} = 0.9\,\mathrm{Hz}$ for the non-linear weakly dispersive reconstruction.

Quantity	ζ_{lidar}	ζ_{hyd}	$\zeta_{\mathrm{lin,\,f_c}}$	ζ_{snl}
Variance [m^2]	0.073	0.054	0.069	0.073
Variance error	-	25.5%	5.8%	0%
S_k [-]	1.81	1.00	1.21	1.70
S_k error	-	44.3%	33.1%	5.9%
A_s [-]	-0.52	-0.29	-0.36	-0.43
A_s error	-	43.9%	30.5%	16.2%

Table 3. Relative errors made by the different reconstruction methods for the inner surf zone burst (Figure 8b, $h_0 = 0.76\,\mathrm{m}$, $\mu = 0.17$ and $H_s = 0.44\,\mathrm{m}$). For this burst, the cutoff frequencies used are $f_{\mathrm{c,\,lin}} = 0.5\,\mathrm{Hz}$ for the linear reconstruction and $f_{\mathrm{c,\,snl}} = 1.1\,\mathrm{Hz}$ for the non-linear weakly dispersive reconstruction.

Quantity	ζ_{lidar}	ζ_{hyd}	$\zeta_{\mathrm{lin,\,f_c}}$	ζ_{snl}
Variance [m^2]	0.012	0.011	0.012	0.013
Variance error	-	8.1%	1.7%	4.3%
S_k [-]	0.75	0.52	0.56	0.80
S_k error	-	31.1%	25.4%	6.9%
A_s [-]	-1.07	-0.79	-0.88	-1.05
A_s error	-	25.8%	17.6%	1.6%

1019 # Figures

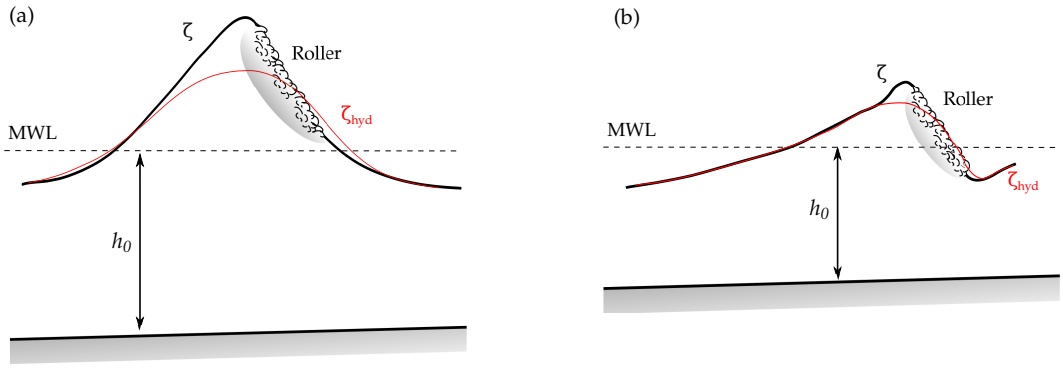

Figure 1. Illustrative sketch of the free surface elevation for surf zone waves propagating in the outer (a) and inner (b) surf zones. ζ represents the free surface elevation while ζ_{hyd} corresponds to the surface elevation reconstructed with the hypothesis that the pressure field is hydrostatic. MWL refers to the Mean Water Level while h_0 is the mean water depth. Note that for plunging cases, the situation is more complex than depicted in panel (a), but effectively, the breaking wave can exhibit such shape after the splash-up phase. Near the breaking point, the overestimation of the free surface elevation by ζ_{hyd} in front of the wave face is even more pronounced (see for instance Figure 2 in Martins et al., 2017a).

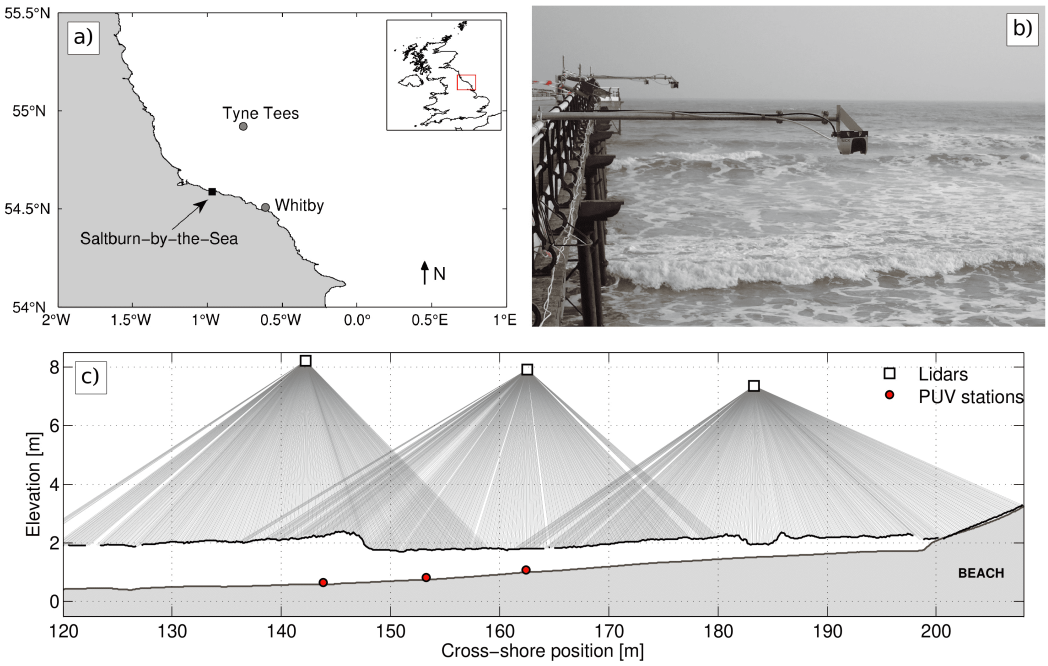

Figure 2. Field site and lidar scanner deployment during the April 2016 experiments at Saltburn-by-the-Sea, UK (modified from Martins et al., 2018). Panel (a) shows the regional map around Saltburn and the location of nearshore (Whitby) and offshore (Tyne Tees) wave buoys (grey dots). The lidar scanner deployment on the nearshore pier is depicted in panel (b): the scanners were deployed 2.5 m away from the pier, using a 'T'-shaped scaffolding system directly fixed to the pier railing. Panel (c) presents a schematic of the experimental setup with an example of post-processed free surface elevation (black thick line while individual measurements are shown as light grey lines). The beach profile (thick grey line) corresponds to the surveyed profile during the previous low tide (10 April 2016).

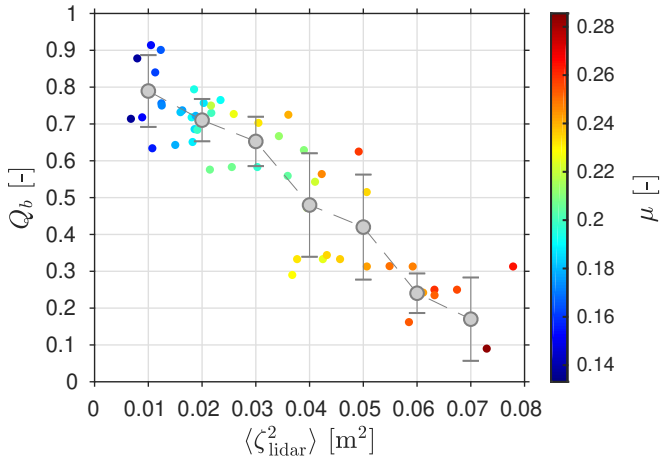

Figure 3. Fraction of breaking and broken waves Q_b at the most offshore ADV location as a function of the surface elevation variance $\langle \zeta^2_{\mathrm{lidar}} \rangle$ computed on the lidar data. Individual burst data point are coloured by the value of the relative water depth μ over that particular burst. Binned data (mean and standard deviation shown every $0.01\,\mathrm{m}^2$) are shown as grey dots and associated vertical bars.

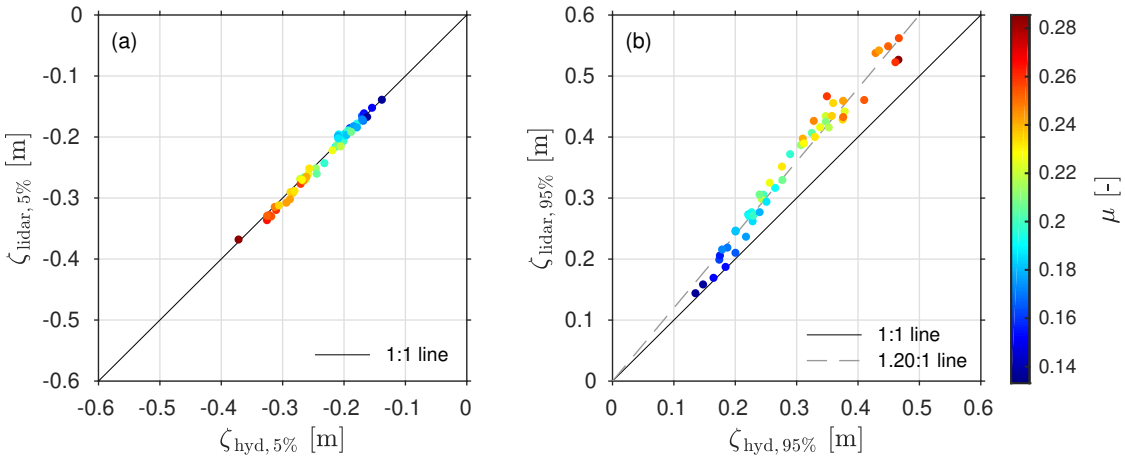

Figure 4. Comparison of the 5% (panel a) and 95% (panel b) surface elevation percentiles computed on the reconstructed signal ζ_{hyd} with the direct lidar measurements ζ_{lidar}. Individual burst data point are coloured by the value of the relative water depth μ over that particular burst.

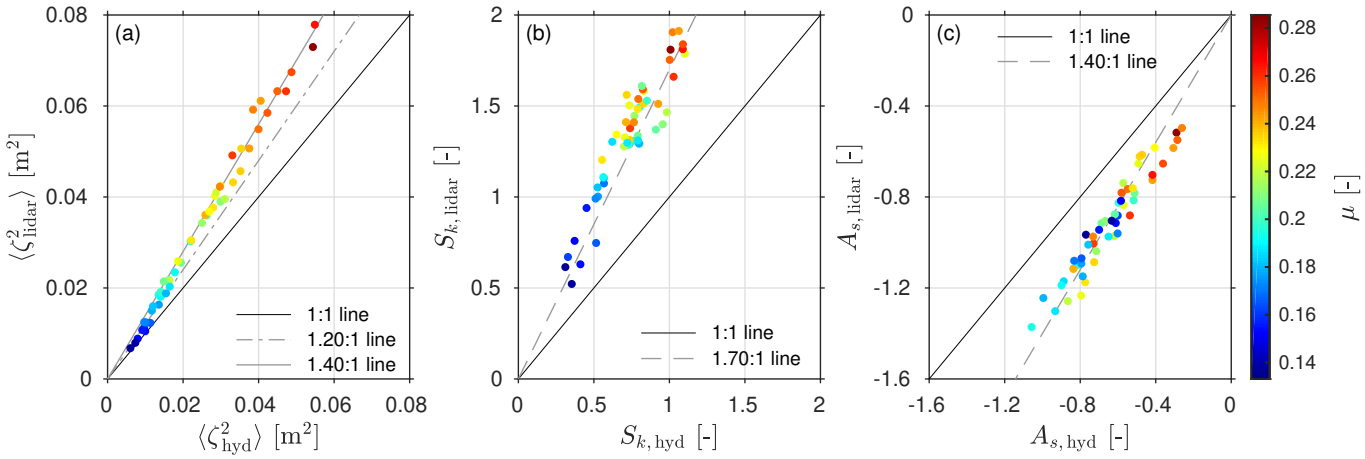

Figure 5. Comparison of second and third-order bulk parameters computed on the reconstructed surface elevation ζ_{hyd} with the direct lidar measurements ζ_{lidar}. Panel (a) shows the variance of the surface elevation (wave energy) while panel (b) and (c) show the comparisons between the surface elevation skewness and asymmetry respectively. Individual burst data point are coloured by the value of the relative water depth μ over that particular burst.

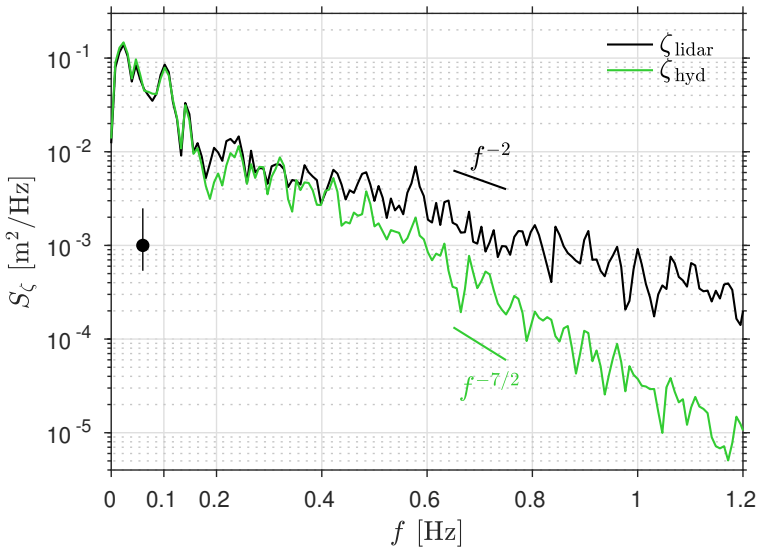

Figure 6. Energy density spectra S_ζ of the reconstructed ζ_{hyd} and directly measured ζ_{lidar} surface elevation signals for the inner surf zone burst. Spectra were computed using Welch's method with 7 Hann-windowed, 128 second segments overlapping by 50%, which results in energy density spectral estimates having approximately 13 degrees of freedom and a spectral resolution of 0.0078 Hz. The 90% confidence interval is shown as the black dot with the vertical bars

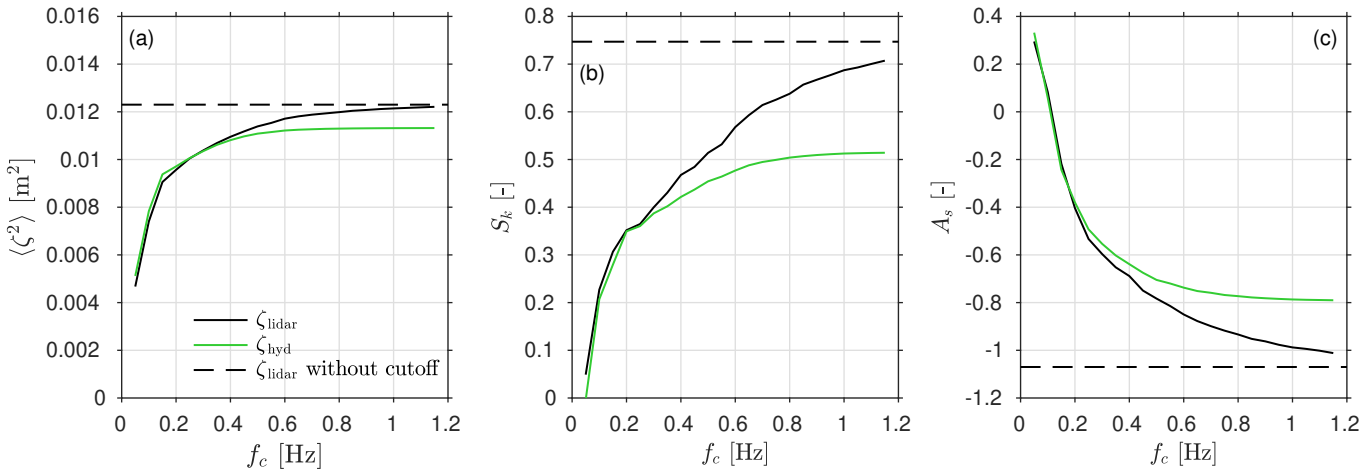

Figure 7. Second and third-order surface elevation parameters for the inner surf zone burst, computed with different cutoff frequency f_c and the original lidar signal. Panel (a) shows the variance while the skewness and asymmetry are shown in panels (b) and (c) respectively.

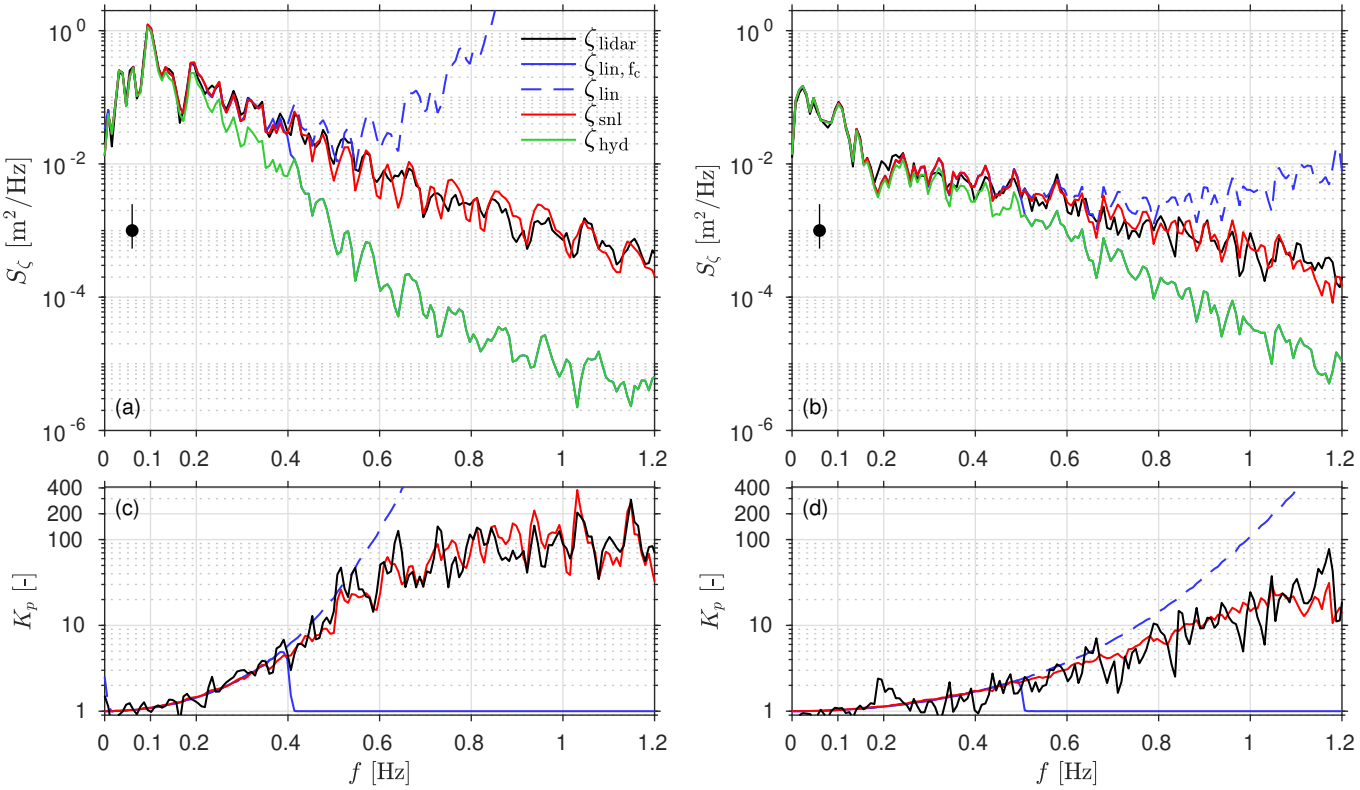

Figure 8. Energy density spectra S_ζ of the reconstructed ζ_{hyd}, $\zeta_{\mathrm{lin,f_c}}$, ζ_{lin}, ζ_{snl} and directly measured ζ_{lidar} surface elevation signals for two contrasting cases: (a) outer surf zone, and (b) inner surf zone. For both cases, the equivalent transfer function K_p for each reconstruction methods is shown below the corresponding panel (c: outer surf zone, and d: inner surf zone). $\zeta_{\mathrm{lin,f_c}}$ corresponds to the linear reconstruction with a cutoff frequency of $f_{c,\mathrm{lin}} = 0.4$ Hz in the outer surf zone and $f_{c,\mathrm{lin}} = 0.5$ Hz in the inner surf zone. The cutoff frequencies for the non-linear weakly dispersive reconstruction are $f_{c,\mathrm{snl}} = 0.9$ Hz in the outer surf zone and $f_{c,\mathrm{lin}} = 1.1$ Hz in the inner surf zone. Note that in panels (c) and (d), the black line corresponds to the observed transfer function $S_{\zeta,\mathrm{lidar}}/S_{\zeta,\mathrm{hyd}}$. Spectra were computed using Welch's method with 7 Hann-windowed, 128 second segments overlapping by 50%, which results in energy density spectral estimates having approximately 13 degrees of freedom and a spectral resolution of 0.0078 Hz. The 90% confidence interval is shown as the black dot with the vertical bars.

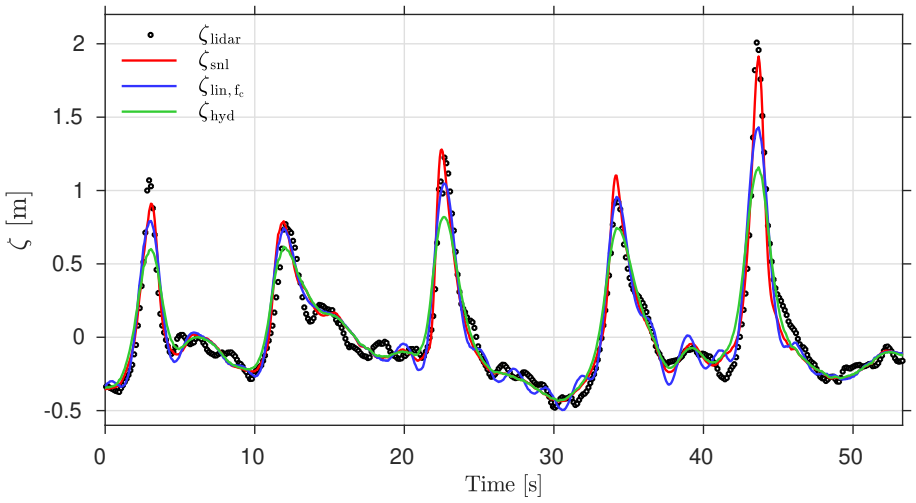

Figure 9. Surface elevation reconstructions and direct lidar measurements for a wave group extracted from the outer surf zone burst. The cutoff frequencies for this example are $f_{\mathrm{c,\,lin}} = 0.4\,\mathrm{Hz}$ and $f_{\mathrm{c,\,snl}} = 0.9\,\mathrm{Hz}$. For readability, lidar data is shown every two points.

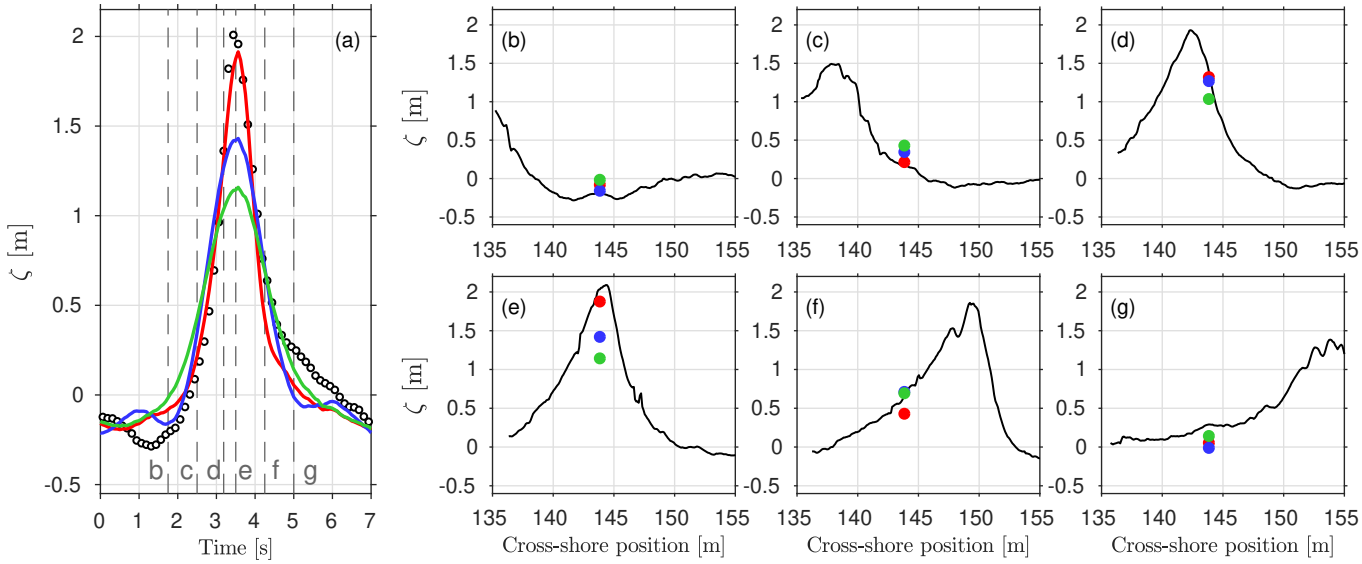

Figure 10. Surface elevation reconstructions and lidar measurements for the extreme wave extracted from the group presented in Figure 9. Panel (a) shows the free surface elevation time series (same color code as Figure 9: circles are for lidar data while red, blue and green lines are for ζ_{snl}, $\zeta_{\mathrm{lin,\,f_c}}$ and ζ_{hyd} respectively). Panels (b) to (g) display the spatial information from the lidar data (black line) along with the corresponding pressure-derived data points (same color code as panel a) at 6 specific moments, indicated in panel (a) as gray dashed vertical lines. The cutoff frequencies for this example are $f_{\mathrm{c,\,lin}} = 0.4\,\mathrm{Hz}$ and $f_{\mathrm{c,\,snl}} = 0.9\,\mathrm{Hz}$.

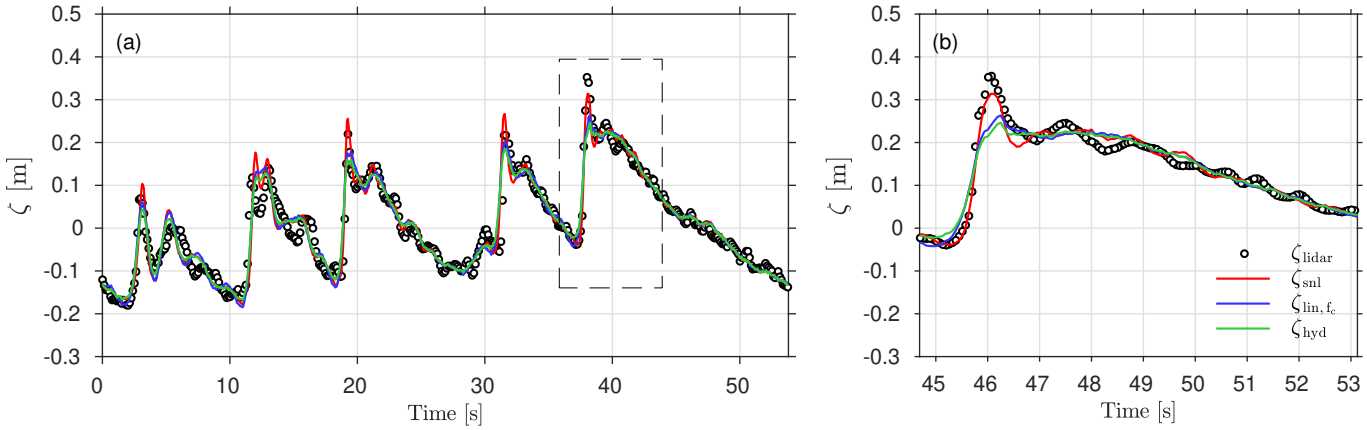

Figure 11. Surface elevation reconstructions and direct lidar measurements for a group of broken waves propagating in the inner surf zone. Panel (a) shows the free surface elevation time series over the group while panel (b) shows a zoom around the largest wave of the group (the corresponding wave is highlighted with the dashed rectangle in panel a). The cutoff frequencies for this example are $f_{c,\,\mathrm{lin}} = 0.5\,\mathrm{Hz}$ and $f_{c,\,\mathrm{snl}} = 1.1\,\mathrm{Hz}$. For readability, lidar data is shown every two points in panel a.

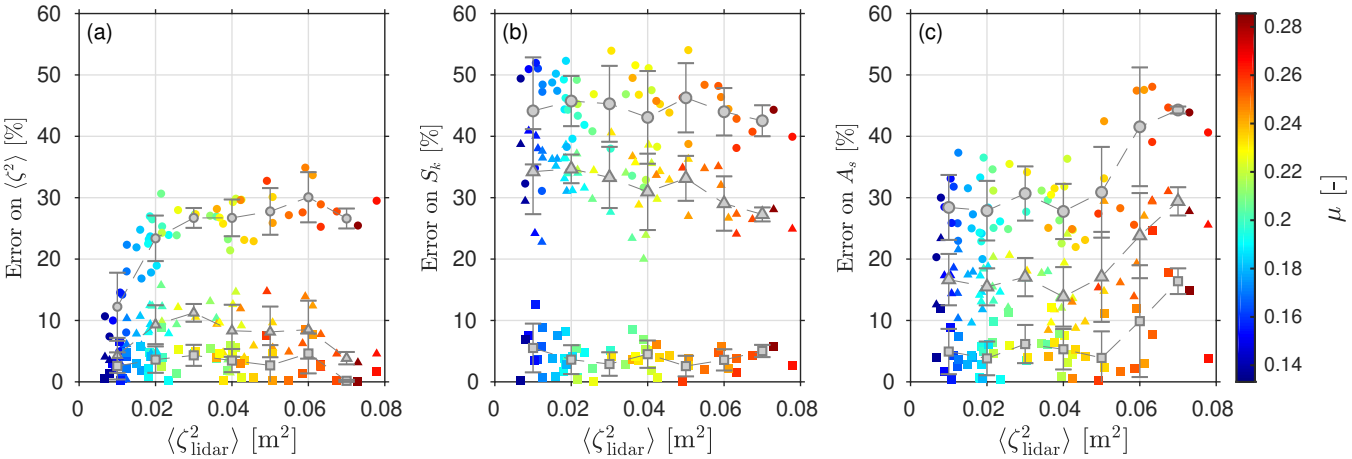

Figure 12. Error made on the surface elevation variance (Panel a), skewness (Panel b) and asymmetry (Panel c) by the different reconstruction methods for every burst of the present dataset. Squares correspond to ζ_{snl} data points while triangles and dots are for $\zeta_{\mathrm{lin,\,f_c}}$ and ζ_{hyd} respectively. Individual burst data point are coloured by the value of the relative water depth μ over that particular burst. Binned data (mean and standard deviation shown every $0.01\,\mathrm{m}^2$) are shown as grey dots and associated vertical bars.

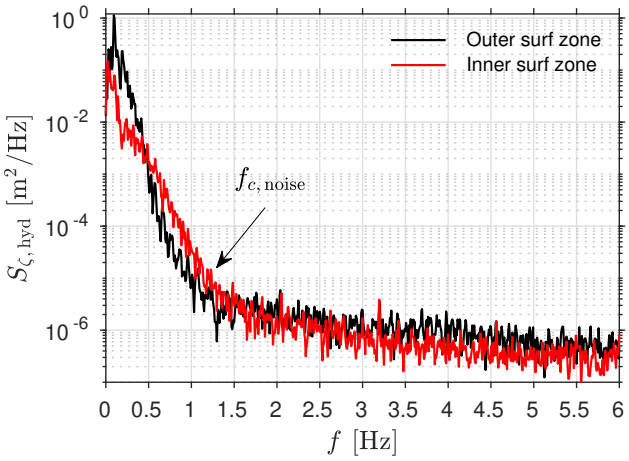

Figure A1. Energy density spectra for the outer and inner surf cases, shown up to 6 Hz. The noise starts to dominate at frequencies higher than approximately 1.2 Hz.

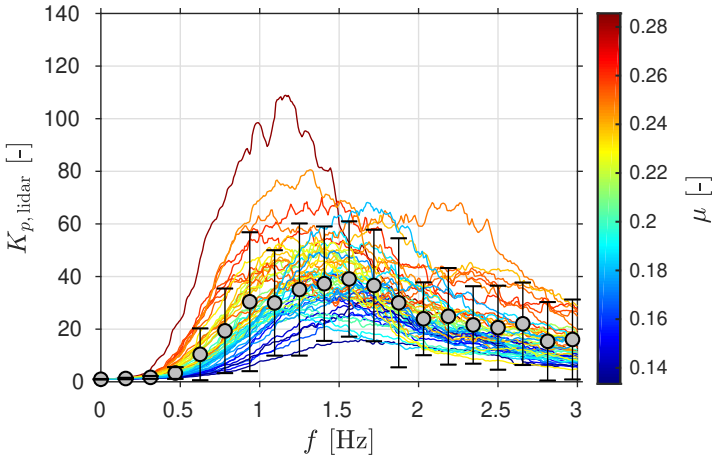

Figure A2. Ratio $K_{p,\,\mathrm{lidar}} = S_{\zeta,\,\mathrm{lidar}}/S_{\zeta,\,\mathrm{hyd}}$ for every burst. As the energy density spectra are quite peaky, the ratio were window-averaged using a window 0.5 Hz-wide. Each line corresponds to a burst and was coloured by the value of the relative depth μ during this burst. Binned data (mean and standard deviation shown every 0.15 Hz) are shown as grey dots and associated vertical bars.